AN INVERSION MODEL OF RECEIVER FUNCTION FOR MOHO DEPTH DETERMINATION BENEATH LOCATIONS OF THE ETHIOPIAN SEISMIC NETWORK STATIONS AND THEIR SURROUNDINGS

By

BIRHANU ABERA

A thesis submitted to the School of Graduate Studies of Addis Ababa University in partial fulfillment of the requirements for the degree of Masters of Science

in

Geophysics

SCHOOL OF EARTH SCIENCES

June 29, 2016

DEDICATIONS

Hiwot Tadesse
Loza Birhanu

ADDIS ABABA UNIVERSITY
SCHOOL OF EARTH SCIENCES
SCHOOL OF GRADUATE STUDIES

AN INVERSION MODEL OF RECEIVER FUNCTIONS FOR MOHO DEPTH DETERMINATION BENEATH LOCATIONS OF THE ETHIOPIAN SEISMIC NETWORK STATIONS AND THEIR SURROUNDINGS

By

BIRHANU ABERA

June 29, 2016

College of Natural and Computational Sciences
School of Graduate Studies

Approval by board of examiners	**Signature**
Dr. Balemual Atnafu	Signature of Chairman
(Chairman)	....
Dr. Atalay Ayele	Signature of Advisor
(Advisor)	....
Prof. Tilahun Mamo	Signature of Examiner
(Examiner)	....
Dr. Elias Lewi	Signature of Examiner
(Examiner)	....

Abstract

Moho depths or crustal thicknesses at four stations of the Ethiopian Seismic Station Network (ESSN) are estimated from Receiver Functions studies. We used high quality seismic data recorded at ANKE (Ankober), DILA (Dila), HARE (Harar) and SEME (Semera) stations for earthquakes located at epicentral distances ranging from 30^o to 100^o and magnitude $M \geq 5.5$. We applied frequency domain deconvolution technique to remove all effects from the earthquakes source and propagation path to make the RFs dependent only on the structure beneath the seismic stations. A linearized-iterative inversion is applied on the generated radial component of the Receiver functions. From the four stations in the study, the minimum number of teleseismic earthquakes is 14 for Harar while the maximum is 39 for Ankober. The estimated values for the Moho depth are $42 \pm 1.7km$, $36 \pm 2km$, $38 \pm 2km$ and $26 \pm 2km$ for Ankober, Dila, Harar and Semera respectively. We have achieved a reasonably good fit between the observed and synthetic RFs which demonstrates the goodness of the inversion. The lowest Moho depth is observed for Semera station which implies a thinned crust while the highest crustal thickness is achieved for Ankober that lies along the western plateau margin. The second low Moho depth is calculated for Dila station while the one for Harar is an intermediate one. Our results agree with previous observations which strengthens the fact that Moho depths estimated for stations that lie within the rift and rift margins are lower than those located in the plateaus. On the other hand, our RFs inversions show low velocity gradient at about $15km$ depth at Semera stations while high velocity gradient is noticed at Ankober station. This may imply a cooled magma from previous dike or sill intrusions beneath Ankober station while the observation at Semera indicates the existence of melt at that depth.

ACKNOWLEDGMENTS

First of all, I would like to thank Dr. Atalay Ayele for his proper guidance throughout the study.
I am indebted to the staff of the Institute of Geophysics Space Science and Astronomy, Addis Ababa University especially Sisay Alemayehu who gave me seismic data and softwares. Similarly, I would like to acknowledge Berhanu Bekele who supported me in preparing location map.

DECLARATION

I declare that the thesis is my original work except for quotations and citations which have been duly acknowledged. I also declare that it has not been previously, and is not concurrently, submitted for any other degree at Addis Ababa University or at any other institution.

Birhanu Abera

Date: June 29, 2016

CONTENTS

LIST OF TABLES

LIST OF FIGURES

ACRONYMS AND ABBREVIATIONS

RFs	Receiver Functions
EQD	Earthquake data
P-wave	Primary wave
S-wave	shear wave
MER	Main Ethiopian Rift
NMER	Northern Main Ethiopian Rift
ANKE	Ankober station
SEME	Semera station
DILA	Dila station
HARE	Harar station
H	Depth to Moho
1-D	One Dimension
2-D	Two Dimension
3-D	Three Dimension
IGSSA	Institute of Geophysics Space Science and Astronomy
FFT	Fast Fourier Transform
RMS	Root Mean Square
MT	Magneto Telluric
Ma	Million years
Ps	Converted P wave to S wave
Pv	Converted P wave to V wave
EAGLE	Ethiopia Afar Geoscientific Lithospheric Experiment
PQL	PASSCAL Quick Look
PASSCAL	Program for Array Seismic Studies of the Continental Lithosphere
SEISAN	Seismic Analysis System
SAC	Seismic Code Analysis
GIS	Geographical information systems
pwaveqn	P wave source equalization
icmod	Inverting code results to wave form
snglinv	Single Inversion
smthinv	Smooth Inversion
manyinv	Many inversion

CHAPTER 1

INTRODUCTION

1.1 Background

Afar and Main Ethiopian Rift are the most studied areas in Ethiopia. There are four classifications of the region in the rift and surrounding plateaus based on the waveform characteristics (Hammond et al., 2011). These are Western-Plateau, Southeastern-Plateau, Southern and Central-Afar, and Northern-Afar. Our stations are located in each of the above regions. Afar is in the processes of transition from continental rifting to the formation of new oceanic crust. There are variations in crustal structure and seismic properties that result from transition in Afar (Buck, 2004). The Ethiopian rift (ER) system that separates the African (Nubian) plate from the Somalian plate has three major rift parts(the Afar Depression, the Main Ethiopian Rift (MER) and the Southern Ethiopian Rift (SER).) and it is bounded by adjacent western and eastern plateaus. Two of our study areas are located in the African (Nubian) plate (i.e Ankober, western Ethiopian plateau) and Somalian plate (i.e Harar and Dilla, eastern Ethiopian plateau). Semera, located in Afar, is one of the seismically and volcanically active rift systems that has been a target of researchers from an early stage of continental break-up to incipient sea-floor spreading in one geodynamic setting (e.g. Mohr, 1967; Bilham et al., 1999; Ebinger and Casey, 2001). The major controlling factor of the continental break-up process is the continuous injection of magma into the crust below the along axis magmatic segments (Keranen et al., 2004; Bastow et al., 2005). The exact rift extension direction, on the other hand, is unclear. With the majority of results showing rift oblique extension direction (e.g. Boccletti et al., 1998; Bilham et al., 1999; Wolfenden et al., 2004) some studies obtained extension directions orthogonal to the Main Ethiopian Rift (MER) orientation (Chorowicz et al., 1994). The Moho interface is a zone of weakness with low viscosity and as such acts as a favorite zone to accommodate the rising melt (Mammo, 2013). The receiver function method is an excellent method for detecting seismic discontinuities such as Moho within the lithosphere and the deeper upper mantle by analysing Ps conversions. It is a time series method to model crust and upper mantle structure from teleseismic wave forms recorded at three component seismic station. It is an important seismological technique in the seismic investigation of the crust and upper mantle (Langston, 1977). It describes the tendency of a P wave, as it ascends toward a seismometer through the layers of the shallow Earth, to show a chain of P-to-S converted waves that accompany the reverberations of the main compressional wave. Owing to the large velocity contrast across the discontinuity, part of the incoming teleseismic P wave energy will convert into SV wave at the Moho. By measuring the time separation between the direct P arrival and the conversion phase, the crustal thickness can then be estimated. The estimation provides a good "point" measurement at the station because of the steep incidence angle of the teleseismic P wave (Zhu and Kanamori, 2000).

This study is mainly concerned with the estimation of crustal thickness and Moho depth in Semera (Afar), Ankober (Western-plateau), Harar (Eastern-plateau) and Dilla (South-Eastern plateau). Afar has a crustal thickness of $20 - 26km$ but thins northward (Hammond et al. 2011). The crustal thickness of Ethiopian plateaus is about $44km$ beneath the western plateau and about $35km$ towards the southeastern plateau. The western plateau is likely associated with Cenozoic flood basalts or current magmatism, whereas the southeastern plateau is typical of silicic continental crust (Hammond et al., 2011).

The main focus of this work is to estimate the Moho depth beneath Semera (Central Afar), Ankober(North western plateau), Harer (Easern Plateau) and Dila(Southern Plateau) using teleseismic data which were collected from January 2014 to June 2015 in Ethiopian permanent broad seismic stations.

1.2 Geology and Tectonics

The Afar Depression is triangular in shape and is separated from the elevated areas of the Ethiopian Plateau to the west, the Southeast Plateau and Ogaden to the south, and the Danakil Horst to the east by fault controlled escarpments. At the southwestern apex of the triangle the East African Rift joins the depression. In the plateaus adjoining the Afar Depression, Mesozoic and Precambrian rocks outcrop, covered on the Ethiopian Plateau by extensive Tertiary volcanic flows. The floor of the depression is covered by several series of Quatemary volcanics with some Pleistocene lacustrine deposits. In the north of the depression thick evaporitic deposits are exposed, covering several thousand square kilometres. A series of active volcanoes exists in the depression, providing spectacular outbursts from time to time (Makris and Ginzburg, 1987). The northern Main Ethiopian Rift was formed within the Precambrian Crustal Basement. The region is covered by marine sediments that were deposited uncomfortably on the Precambrian Basement (Tefera et al.,1996; Cornwell, 2010). Ethiopian Plateau followed the flood basalt eruption from ~29 to ~25 Ma and possibly continued episodically to the present day (Pik et al., 2003; Gani et al., 2007).
A hot mantle upwelling impacting onto the base of the lithosphere is believed to have initiated volcanism in southwestern Ethiopia in the range of $\sim 45 - 40$ Ma (Ebinger et al., 1993)) and in northern Ethiopia where flood basalts cover an area of about 600,000km^2 (Mohr, 1983) and consist of a $< 2km$ layer of bimodal basalt-rhyolite volcanic rocks (e.g., Ayalew et al., 2002; Ayalew and Yirgu, 2003). The flood basalts are thought to have erupted very rapidly (within 1 Myr) throughout northern Ethiopia at ~30 Ma (Hofmann et al., 1997). Uplift of the Ethiopian Plateau followed the flood basalt eruption from ~29 to ~25 Ma (Pik et al., 2003) and possibly continued episodically to the present day (Gani et al., 2007).
In relation to the cross rift profile the middle and upper crust velocities varying from ~6.1 km/s beneath the rift flanks to ~6.6 beneath axial zones of intense Qua-

ternary volcanic activity, interpreted as cooled gabbroic bodies along the current rift axis. Similarly, a high-velocity ($V_p \approx 7.4\frac{km}{s}$) is at lower crustal layer beneath the northwestern rift flank, interpreted as Oligocene mafic material emplaced at the base of the crust (underplate) (Maguire et al. 2006 and Cornwell et al.2010).
The earliest rifting in this region occurred ~ 35 Ma in the Gulf of Aden, post-dating onset of volcanism on the Ethiopian plateau at ~ 40 Ma [Davidson and Rex,1980; Ebinger et al., 1993]. The highest eruption rates coincided with the onset of extension in the southern Red Sea in Afar (Wolfenden et al., 2005). The volcanism is associated with the inland Red Sea rift youngs to the south, and reached $\sim 10^o$N ~ 10 Million years ago (Wolfenden et al., 2004). The third arm of the triple junction, the Main Ethiopian Rift, propagated northward from southern Ethiopia ~ 18 Million years ago (WoldeGabriel et al., 1990) and propagated into the Southern Red Sea rift at $\sim 10^o$N 11 Million years ago (Wolfenden et al., 2004). Thus, no triple junction existed in this region until ~ 20 Ma after the emplacement of the flood basalts and the initial breakup forming the Red Sea and Gulf of Aden.
The tectonic and geodynamic setting of Ethiopian rift has been studied. According to Dugda et al., 2006 extension in rheologically layered continental lithosphere in Afar grouped into two categories:

1. those invoking mechanical stretching, where strain is accommodated by large offset faults in a brittle upper crust and by ductile deformation in the lower crust; and
2. those invoking extension caused by dyke intrusion within magmatic segments (e.g. Ebinger and Casey, 2001; Buck, 2004)

1.3 Location of The Study Area

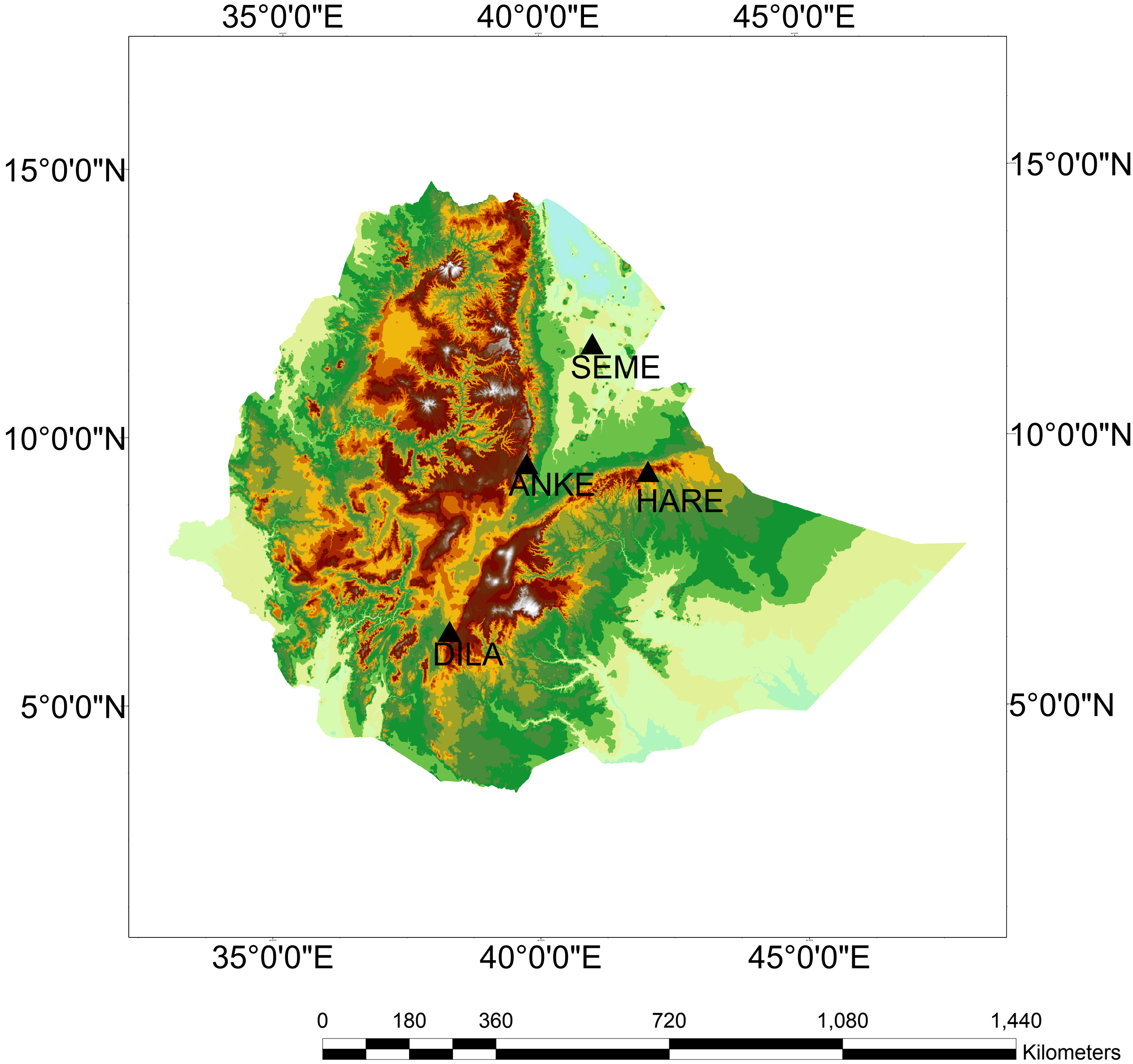

Figure 1.1: Location map of ANKE, DILA, HARE and SEME.

The study areas are located in Afar ($11.8075^o N, 40.9953^o$E), Ankober ($9.583^o N, 39.742^o E$), Harar ($9.4248^o N, 42.0312^o E$) and Dilla ($6.4344^o N, 38.2866^o E$).

1.4 Statement Of The Problem

Generating artificial seismic source is an expensive method when it is compared with natural seismic source. For instance, hexanitrostilbene is the main explosive seismic source filled in a drilled hole. The intensity of the seismic waves' is proportional to weight of the applied explosive. To study Lithospheric structure seismic refraction experiment is a reliable method that gives accurate estimation of crustal thickness and compressional velocity. But, this method needs detailed data analysis and extensive modeling of both travel times and amplitudes of crustal body waves. The cost of such surveys is often very high, and their spatial coverage is very limited. An alternative and more effective technique of estimating Moho depth is to use teleseismic RFs. Wide-angle reflection and refraction seismic waves travel long distance laterally within the crust and they are much more sensitive to lateral velocity variations than to the Moho depth variations.

1.5 Objectives Of The Study

1.5.1 General Objective

The general objective of this work is to develop a model of crustal structure beneath Afar and Rift adjoining plateaus using an inversion of teleseismic wave form Receiver Functions.

1.5.2 Specific Objectives

The specific objectives of this work is:

- To apply passive seismic method for Moho depth estimation and crustal compositions;

- To determine depth to Moho and map laterally varying crustal thickness;
- To determine laterally varying vertical velocity gradients;
- To substantiate previous results given to causes of Ethiopian rifting;
- To comapre Moho depth between adjacent plateaus.

1.6 Significance of The Study

RFs method is an alternative and effective technique to estimate Moho depth.

- RFs method could be an alternative technique to estimate Moho depth.
- This study can be a reference work for those who want to take on crustal and Moho-depth determination in addition to another seismological methods.
- The work will be an additional estimate of Moho depth that used seismic source for the study of crustal structure (e.g Ayele, 2004; Dugda, 2005; Hammond, 2011).
- The study validates previous 1D crustal and Moho-depth models.
- The study can be a supporting document for future researchers for those who want to customize Fortran codes and use the codes as a subroutine for future use crustal and Moho depth determination.
- The result can be used as an input for future Moho depth map of Ethiopian Rift and the surrounding plateaus.

CHAPTER 2

LITERATURE REVIEW

Moho is defined as an increase of Vp to 7.4 km/s. Crustal structure beneath Djibouti has been characterized to be $23 \pm 1.5km$ and a mean Vp of $6.2km/s$. The crustal structure of certain places in Djibouti is similar to crustal structure in many other parts of central and eastern Afar (e.g Dugda et al., 2006). Ruegg (1975) interpreted the Moho depth posses velocities between 6.4 km/s and 6.9km/s (i.e. velocities of about 6.9 km/s and higher were considered to be indicative of mantle rock). Makris and Ginzburg (1987) interpret P-wave velocities as high as 7.1 - 7.2 km/s as crustal velocities, and they concluded that the Moho is marked by an increase in velocity to 7.5 km/s. Average crustal Vp values for rifted continental crust is about 5.8 - 6.8 km/s (Prodehl et al. 1994 and references therein). Continental rifts often evolve in settings with heterogeneous crust and lithosphere (Dugda et al., 2006). The heterogeneity may be added as the rift develops, such as the addition of magmatic material to the crust. Magma injection has probably replaced mechanical failure as the main strain accommodation mechanism (Ebinger and Casey, 2001). A hot mantle upwelling onto the base of the lithosphere is believed to have initiated volcanism in southwestern Ethiopia (45-40 Ma (Ebinger et al., 1993)) and in northern Ethiopia where flood basalts cover an area of about 600,000 km^2 (Mohr, 1983). A process of diking/veining affects the crust and lithospheric mantle in the NMER to a depth of at least 30 km (Rooney et al., 2005; Cornwell et al., 2010). Related to the Cross Rift profile, middle and upper crust velocities varying from $\sim 6.1km/s$ beneath the rift flanks to $\sim 6.6km/s$ beneath axial zones of intense Quaternary volcanic activity. This is interpreted as cooled gabbroic bodies along the current rift axis. A high-velocity with Vp $\sim 7.4km/s$ along the lower crustal layer beneath the northwestern rift flank is interpreted as Oligocene mafic material emplaced at the base of the crust (underplate) (Cornwell et al., 2010 and referenced there in). The western flank of the rift (Nubian plate) generally displays a thicker crust (40 - 43 km) than the eastern flank (Somalian plate) (38 - 40 km) (Cornwell et al., 2010). White et al. (2008), adding a magmatic intrusive material a P wave velocity of 7.3 km/s requires a positive mantle temperature anomaly of 150 - 175 K. If this hot material is emplaced into the lower crust it would raise the regional geotherm and partially melt portions of it. Annen and Sparks (2002) basalt sill intrusion into the lower crust control the generation of melt by:-

1. the rate of magma intrusion,

2. the composition and water content of the preexisting crustal rocks, and

3. the temperature and water content of the intruding basalt magma.

Melt generation involves simultaneous cooling and crystallization of intruding magma and partial melting of both new mafic crust and the preexisting old crust. The proportion of these components depends on the fertility of the crust and the temperature and water content of the mafic magma (Furman et al., 2006; cornwell, 2010). Rifting is located where the least amount of magma has been emplaced into the lower crust. The processes of localized dike intrusion with underplating would produce strips of mafic crust transitional to oceanic crust (Ebinger et al., 2001). Lower crustal earthquakes are commonly observed in continental rifts at depths where temperatures should be too high for brittle failure to occur. Earthquakes occur on the broad western margin of the MER and beneath the NW plateau, with almost no earthquakes recorded beneath the SE Plateau (Keir et al., 2009). The mantle beneath the NW plateau is among the slowest worldwide (Bastow et al., 2008). Low velocity anomaly cannot be explained by variations in composition and temperature alone. It requires the presence of a small fraction fluid phase, which is likely to be partial melt. MER is unaffected by subduction processes that could hydrate the mantle [Bastow et al., 2005; Bastow et al., 2008 and Keir et al., 2009]. Crust beneath the NW Plateau is generally 40 - 50km thick. Across the broad western rift margin, the crust includes a 10km-thick, high-density and high P wave velocity (Vp) (7.4 - 7.7km/s) at the lower most crust which is interpreted as gabbroic (Mackenzie et al., 2005; Cornwell et al., 2006 and Maguire et al., 2006). In the work of Makris and Ginzburg (1987), the seismic refraction result obtained at Profile I (Ethiopian Plateau) was 3.75 km/s corresponding to the volcanic rocks and sedimentary cover, 6.1 km/s for the upper crust, 6.65 km/s for the lower crust and 8.0 km/s for the upper mantle. Incontrast, in the south western Afar Depression, the a P wave velocity results are 2.8 km/s (Pleistocene sediments in Lake Hertale, 4.1 km/s (volcanics), 6.1 km/s (upper crust), 6.7 km/s (lower crust) and 7.4 km/s (anomalous mantle) (Makris and Ginzburg, 1987). This event was interpreted as a reflection from the top of the normal 8.0 km/s upper mantle at a depth of 45.0 km. In addition to the above profiles, the south western end of the profile shows a 2.5 km thick layer with P wave velocity of 2.2 km/s young sediments overlies the basalt cover. The lower crust with a velocity of 6.6 km/s at a depth of 26.0 km overlying a 7.5 km/s upper mantle (Makris and Ginzburg, 1987). Finally, central part of the depression, near Dallol another thick accumulation of low velocity (3.35 km/s) material which represents sediments and evaporites (Behle et al., 1975) overlies the basalt series (4.5 km/s). The lower crust-upper mantle represented by a velocity of 7.4 km/s is located at a depth of some 26.0 km in the south. The crust throughout the depression is underlain by an upper mantle with an anomaly low velocity of 7.4 km/s. Under the crust of Afar, the temperature of the upper mantle material is higher than usual which was also indicated by the results of the magnetotelluric soundings carried out in the region (Berktold et al., 1975 and Makris et al., 1987). The south eastern part of Afar depression and Gulf of Tadjura, exhibit low velocities (6.8 - 6.9 km/s), have been interpreted as hot anomalous mantle (Mechie and Prodehl, 1988). Regions close to mid-ocean ridge have high temperatures that are enough to cause a significant reduction of seismic velocity. The uncertainity of Moho depths may come from hot mantle rocks which may have velocities similar to lower crustal rocks at lower temperatures (Mechie and Prodehl, 1988). Within the Afar depression the exposed rocks consist of Tertiary and Quaternary volcanics and sediments. This upper and lower crust underlined by the topmost mantle having velocities of 7.3 - 7.7 km/s. The uppermost mantle of Ethiopian plateau velocity is 8.0 km/s. Different rock types may have the same seismic velocity. An increase in temperature may cause the seismic velocity of a particular rock-type to be different at various locations. Ruegg (1975) stated that velocities ranging from 6.8 - 6.9 km/s were representative of hot anomalous mantle beneath the region around the Gulf of Tadjura. Berckhemer et al. (1975) assigned a velocity of 6.8 km/s to the lower crust in North Afar and in the Gulf of Aden. Laughton and Tramontini (1969) decided that velocities of 7.05 - 7.15 km/s were representative of hot anomalous mantle in the area near the mid-ocean ridge, while velocities of less than 7.0 km/s were representative of the lower crust (Mechie and Prodehl, 1988). In the southern Afar depression, anomalous mantle with 7.2 - 7.3 km/s velocities occurs at depths greater than 25 km (Prodehl and Mechie, 1991). Ruegg (1975) interpreted as the underlying layer with 6.7 - 6.9 km/s velocities as an anomalous low-velocity upper mantle. The crust under the Ethiopian plateau has a typical shield structure and is underlain by a mantle of normal seismic velocity. The anomalous mantle velocities of 7.4 - 7.8 km/s existing under all Afar may be consistent with a solid plagioclase pyrolite or with a peridotite with a few percent melt (Prodehl, 1991). Elevated western plateau section across-rift shows high-velocity (7.4 km/s) lower crustal underplate at depths of 33 - 48 km (Mackenzie et al. 2005 and Stuart et al., 2006). The process of continental break-up is governed by crustal stretching and rifting accompanied by the emplacement of melt into the lower crust above a lower density upper mantle. Throughout Ethiopia the crust appears to have a consistent, laterally continuous layering consisting of lower crust with a P-wave seismic velocity of Vp (6.7 - 7.0 km/s), an upper crust with Vp (6.0 - 6.3 km/s) and cover rocks of lava flows and sediments with Vp (2.2 - 4.5 km/s) (Lewi et al., 2015). Boreholes show that there are 1400 m, 1200 m and 600 m thick sedimentary layers, with intercalations of thin basaltic layers. In general, these boreholes show that the thickness of sediments decreases towards the north and increases towards the centre of the Tendaho Graben (Lewi et al., 2015). The results of other MT surveys in this area (Desissa et al. 2013; Didana et al. 2014 and Lewi et al., 2015) also showed the presence of a highly electrically conductive body that is best explained by the presence of partial melt in the area. The process of crustal stretching and thinning under the central part of the Tendaho Graben is accompanied by magma intrusion. The dykes solidified quickly as a result of heat loss close to the surface, whereas the deeper, lower crustal magma reservoir appears to have remained partially molten for longer periods (Lewi et al., 2015).

2.1 Previous Results From RFs-Method

There were many previous studies done in Ethiopia related to moho depth determination. Few of them employed a Teleseismic Receiver Function (RFs) Method. This method was harnessed using both Forward (e.g Ayele et al. 2004) and Inverse (e.g Dugda et al. 2005) methods to determine crustal thicknesses. Previous studies conducted in the NMER using RFs method determined crustal layers with mafic composition ($\frac{V_p}{V_s} \approx 1.87$) and partial melt ($\frac{V_p}{V_s} \geq 1.87$) (Dugda et al. 2005). Outside of the Ethiopian Rift, the value of $\frac{V_p}{V_s}$ ranged from $1.71\frac{km}{s} - 1.81\frac{km}{s}$, were concluded to be crust that has not been modified greatly by cenozoic rifting and volcanism (Cornwell et al., 2010 and Stuart et al., 2006).

The cover rock layer of the Ethiopian Rift is sediments and volcanics having P wave velocity ranging from $2.2\frac{km}{s} - 4.5\frac{km}{s}$. The upper crustal layer of the Rift has a Pwave velocity of $6.0\frac{km}{s} - 6.3\frac{km}{s}$. In addition to this the lower crust P wave velocity is ranging $6.7\frac{km}{s} - 7.0\frac{km}{s}$ above a relatively low velocity mantle having a P wave velocity between $7.4\frac{km}{s} - 7.6\frac{km}{s}$ (Prodehl and Mechie, 1991; Hammond et al., 2011). Undistinguishably to the velocity results, the crustal thickness of western flank of the rift (Nubian plate) depleted as $\sim 40km$ to ~ 43 km and the eastern flank (Somalian plate) get hold of $\sim 38km$ to $\sim 40km$ (Cornwell et al. 2010). The crust in Afar and MER is approximated by a three layer model (Hammond et al.,2011 and Prodehl et al., 1991). These modeles are:

1. The cover rock layer around the rift which is sediments and volcanics having P wave velocity ranging from $2.2\frac{km}{s} - 4.5\frac{km}{s}$ and an upper crust ranging Pwave velocity $6.0\frac{km}{s} - 6.3\frac{km}{s}$;

2. The lower crust Pwave velocity that is ranging $6.7\frac{km}{s} - 7.0\frac{km}{s}$ and;

3. Below the lower crust, there is a relatively low velocity mantle having a P wave velocity between $7.4\frac{km}{s} - 7.6\frac{km}{s}$ (Prodehl et al., 1991 and Hammond et al., 2011).

Table 2.1: A Summary of the Findings of Previous Receiver Function Studies in Ethiopia (Cornwell et al. 2010).

Region	Moho Depth (km)	$\frac{V_p}{V_s}$	Poisson's Ratio (s)	Source
Afar	25	2.13	0.36	Dugda et al. [2005]
Main Ethiopian Rift	27 - 38	1.78 - 2.08	0.27 - 0.35	Dugda et al. [2005]
Main Ethiopian Rift	30 - 38	1.85 - 2.10	0.29 - 0.35	Stuart et al. [2006]
Eastern Plateau	37 - 42	1.74 - 1.81	0.25 - 0.28	Dugda et al. [2005]
Eastern Plateau	38 - 40	~1.80	~0.26	Stuart et al. [2006]
Western Plateau	34 - 44	1.71 - 1.81	0.24 - 0.28	Dugda et al. [2005]
Western Plateau	38 - 43	~1.85	~0.28	Stuart et al. [2006]

The cover rocks in Afar are up to 5 km thick (Makris and Ginzburg, 1987). Due to evaporite deposits Behle et al., 1975, Makris and Ginzburg et al., 1987 argue that, the thinned upper crust beneath Afar is not reflected in the lower crust, suggesting that the lower crust is thickened due to the emplacement of magmatic material (Maguire et al., 2006). According to Hammond et al., (2011) directly beneath volcanic segments velocities of elevated upper crustal is about $6.6\frac{km}{s}$. This was interpreted as cooled intruded gabbroic bodies (Keranen et al., 2004; Mackenzie et al., 2005; Cornwell et al., 2006).

The crust beneath MER and western plateau have high $\frac{Vp}{Vs}$ (≥ 1.8) but beneath the south eastern plateau shows typical continental rock type values $\frac{Vp}{Vs} < 1.8$ (Christensen, 1996). These values are averages for the whole crust, thus high $\frac{Vp}{Vs}$ values above 1.9 likely indicate the presence of fluid, most likely partial melt. This, along with the presence of recent seismicity (Keir et al., 2006), Quaternary eruptive centers (Hayward and Ebinger, 1996) and highly conductive bodies (Whaler and Hautot, 2006) interpreted as a conductive lower crust that could be evidence of partial melt. This region has been attributed to ongoing magma injection into the lower and middle crust (Keir et al., 2009). Additional studies of crustal and mantle anisotropy suggest that magma input into the crust increases northward through the MER toward Afar (Ayele et al., 2004; Kendall et al., 2005).

According to Dugda et al., (2006) the Moho in Afar is marked by an increase in velocity to $7.5\frac{km}{s}$. Moho depth of Tendaho (Central Afar) is $25km \pm 3km$ (Dugda et al., 2005).

Mohr et al., 1989 reviewed two models for the transition from continental rifting to sea-floor spreading and nature of Afar crust which have different tectonic origins; These are:-

1. The modification of precambrian continental crust by stretching igneous intrusions.

2. New igneous crust created by the addition of large volumes of mafic magma and lesser amounts of silicic magma capped by flood lavas.

2.2 Previous Results From MT and Gravity Method

Table 2.2: A Summary of the Findings of Previous Gravity Methods Studied in Ethiopia.N, S, E, W are north, south, east and west respectively.

Region	Method Used	Moho Depth(km)	Source
Dallol	2-D gravity Modeling (Bouguer anomaly)	~ 15	Makris et al. [1991]
N. and E. Afar	Gravity Method(Isostatic Compensation Model)	~ 22	Mammo (2004)
Central Afar	Gravity Method(Isostatic Compensation Model)	~ 26	Mammo (2004)
Central Afar	2-D gravity Modeling (Bouguer anomaly)	$18 - 22$	Makris et al. [1991]
S.Afar(Junction with MER)	Gravity Method(Isostatic Compensation Model)	~ 28	Mammo (2004)
S.Afar	2-D gravity Modeling (Bouguer anomaly)	$22 - 25$	Makris et al. [1991]
Plateau	3D Gravity Inversion	36-46(extrusive lava underplating and isostatic adjestment)	Mammo (2013)
W. Plateau	3D Gravity Modeling	39-43	Mahatsente et al. [1999]
W. Plateau	3D Gravity Inversion	38-46 (NWplateau)	Mammo (2013)
NE. Plateau	3D Gravity Modeling	38-42	Mahatsente et al. [1999]
SW. Plateau	3D Gravity Inversion	34-38	Mahatsente et al. [1999]
NE. Plateau	3D Gravity Modeling	34-42	Mahatsente et al. [1999]
SE. Plateau	3D Gravity Inversion	34-38	Mahatsente et al. [1999]
E. edge Plateau	Gravity Field(Bouguer Map)	~ 30	Makris et al. [1972]
S. End Rift	3D Gravity Inversion	~ 38 (S. Most MER)	Mammo (2013)
E. and NE Extrems of Afar	3D Gravity Inversion	18-22	Mammo (2013)
N. End of Rift	3D Gravity Inversion	~ 7	Mammo (2013)
Dobbi, Guma and Gawa grabens	Gravity Field (Bouguer Map)	8	Makris et al. [1972]

Beneath the plateau normal lithospheric mantle was modeled but the mantle beneath Afar and NMER shows low density values due to partial melt emanating from the upper mantle filled cracks and dykes in the crust and mantle beneath MER and Afar(Kendall et al., 2005). Lithospheric mantle seemed destroyed by the upwelling of hot mantle magma intrusions which contributed the extension process (Mammo, 2013). Magma intrusions and intense dyke injections through these fractures further assisted the extension process (Yirgu et al., 2006; Ayele et al., 2007; Keir et al., 2009; Mammo, 2013). The Moho interface is a weakness zone having low viscosity and acts as a convenient zone for the uplifting melt that migrates upward and spreads along the crust-mantle interface as underplate along the border faults and boundaries initiates the rifting process (Mammo., 2013). Magma reservoir at the depth of 15-25km is observed across Tendaho Graben and south-central part of Red Sea (Johnson., 2012 and Lewi., 2015). Sedimentary cover especially alluvial and lacustrine deposits around Tendaho Graben (Aquater (1996); Gianelli et al., 1998 and Lewi et al., 2015). Applying the result of lithological logs from boreholes, Lewi (2015) showed that the thickness of sediments is not more than 1.2 km and decreases northwards to about 0.75 km. Semera is locate north east of Tendaho at a distance of $\sim 14km$. Beneath Tendaho Graben gravity modeling showed low density material (basaltic melt in a magma reservoir) and from MT profile results high electrical conductivity material occupies horizontally $\sim 13km$ extent of width beneath 15-28km depth at the rift axis (Johnson., 2012). Similarly, along south central part of Red Sea Rift, using gravity modeling 13km broad-ranging partial melt is observed at the depth of 8.5 - 25km. Moho rises from a depth of 33km at the western margin of Red Sea Rift to a depth of 25 km underneath the axis of Tendaho Graben (lewi et al., 2015).

2.3 Crustal Structure In Ethiopian Rift and Adjoining Areas

The magmatic underplate beneath the NW plateau increases in the crustal thickness by making the crust stronger and leads to surface uplift after it was cooled (Mammo, 2013). The thermal anomaly causes strain and rheological heterogeneity between the stronger mafic underplate and the weaker felsic crust (Mammo, 2013). Crustal structure beneath the northern Ethiopian rift has been studied using independent tomographic inversion of P- and S-wave relative arrival-time residuals from teleseismic earthquakes recorded by the Ethiopia Afar Geo-scientific Lithospheric Experiment (EAGLE) (Bastow, 2005). According to Dugda et al. (2005) the crustal thickness of Ethiopian rift and Afar depression varies from $25km$ to $31km$. Similarly, the Moho depth of eastern plateau is between $37km - 42km$ and western plateaus varies between $34km - 44km$.

The crust beneath NMER and Afar is extensively altered by Cenozoic rifting and magmatism (Mammo, 2013). Crustal thickness in Ethiopian rift and around ranges from $\sim 45km$ beneath the north western highlands to $\sim 16km$ beneath oceanic spreading center in northern Afar. Afar has a crustal thickness of $20km - 26km$ outside the currently active rift segments and thins northward. The Moho depth beneath western plateau is ($\sim 40km$) and $\frac{Vp}{Vs}$ underneath this area is about $1.7 - 1.9$. This suggests that a mafic altered crust which is likely associated with Cenozoic flood basalts or current magmatism. Likewise, the southeastern plateau has a Moho depth $\sim 35km$ and contains silicic continental crust with $\frac{Vp}{Vs} \sim 1.78$. High $\frac{Vp}{Vs}$ in the lower crust is melt magmatic intrusions which plays an important role in rifting (Hammond et al., 2011). Rifting thins crust and the continual injection of mafic rocks has extensively modified the physical and chemical composition of the original crustal materials including any underplate that may have existed (Mammo, 2013).

Continental rifting is heterogeneous in the composition of lithosphere within which rifting occurs (Ruegg et al., 1975).

Table 2.3: A summary of the findings of previous receiver function studies in Djibouti south of the Gulf of Tadjoura (Ruegg et al., 1975).

Layers	P-wave velocity $\frac{km}{s}$	thickness(km)
1st layer	4	3.6
2nd layer	6.4	5.6
3rd layer	6.9	4.6
4th layer	7.1	11
5th layer	7.4	10

Ruegg et al., 1975 interpreted the Moho to be at about 10-11 km depth with velocities of $6.4\frac{km}{s}$ and $6.9\frac{km}{s}$ (i.e. velocities of about $6.9\frac{km}{s}$ and higher were considered to be indicative of mantle rock. The values for average crustal V_p values for rifted continental crust $5.8\frac{km}{s} - 6.8\frac{km}{s}$ and crustal thickness can vary by almost $4km$ while the $\frac{Vp}{Vs}$ ratio can change by 0.02 (Dugda et al., 2006; Fuchs et al. 1997 and Prodehl et al. 1994). The northwestern sector crustal structure of Afar is thinned and partially molten rocks but a southeastern sector has high velocity and density anomalies which has a Moho "hole" in the crustal magma system. The crustal structure of the southeastern rift flank has an average crustal thickness of 39 km ($\frac{Vp}{Vs} \sim 1.77$), which indicates the crust in this region is from felsic to intermediate composition (Wilson, 2005; Cornwell, 2010). The Main Ethiopian Rift initiated in a Precambrian lithospheric fabric that had been modified by tertiary plume magmatism and then evolved into the present day rift, in which magma injection has probably replaced mechanical failure as the main strain accommodation mechanism (Ebinger and Casey, 2001).

CHAPTER 3

METHODOLOGY

3.1 Receiver Function Technique

Receiver-function methods give 1-D velocity versus depth profiles of the crust and uppermost mantle beneath the receiving station derived from 3-component broadband records of teleseismic earthquakes. As energy from such an earthquake traverses, the seismic velocity discontinuities show the Earths structure on the receiver side, from the analysis of conversion of some energy from P-wave to S-wave propagation. The S-wave energy is recorded predominantly on the horizontal components and may be separated from energy resulting from the source and source-side structure by deconvolving the radial component with the vertical component to remove the signature of the source and instrument responses from the waveforms (Langston, 1979; Ammon, 1991).

Energy converted from P- to S-waves at the Moho discontinuity is often clearly seen on receiver function waveforms. The S-wave travels more slowly through the crust beneath the receiving station and, hence, arrives a few seconds later than the P-wave energy. The amplitude and the width of the Moho peak is related to the nature of the contrast in shear wave speed across the seismic Moho. Modeling the amplitude and timing of those reverberating waves can supply valuable informations on the underlying geology(Langston, 1979, Ammon, 1990 and Ammon, 1991).

Receiver functions are easy to define but difficult to compute in a reliable and robust manner. Favored methods to compute RFs is by spectral division, a ratio of Fourier transforms. The fundamental of this method is that the P waves signal from distant events incident to a discontinuity in the crust or upper mantle will be converted to S waves(Ps). The S-waves travel slower than the P waves, so, a direct measure of the depth of the discontinuity is calculated by the time difference in the arrival of the direct P wave and the converted phase (Ps), provided the velocity model is known. The important one is to isolate P-to-S converted phases that reverberate in the structure beneath the seismometer by using water-level deconvolution (Ammon, 1991 and Amukti, 2015).

Amplitudes, arrival times, and polarity of the Ps-phases are mainly sensitive to the shear wave velocity distribution beneath the station in the receiver function are sensitive to the local earth structural response, and can be obtained using P-to-S converted waves and their reverberations. This method applies deconvolution of P wave from radial component to isolate receiver function response (Ammon, 1990). These converted phases should be rotated into the ray coordinate system to obtain receiver function response. The rotation of the data is taken place from (ZNE) (Z=Vertical, N=North, E=East) to ZRT (Z=Vertical, R=Radial, T=Tangential) component, and deconvolution technique between Radial and Vertical component in time domain that removes the source and travel path effects (Ammon, 1990 and Dugda, 2005). The processed receiver functions provide images of the crust and upper mantle.

It widely applies in deep crustal and upper mantle studies. The inversion technique of receiver function response is used to obtain subsurface structure. Receiver functions from numerous teleseismic earthquakes recorded at Ethiopian broadband seismic stations have been analyzed to map crustal thickness, $\frac{Vp}{Vs}$ ratio and Moho thickness beneath and around the stations. In this study we used the converted P to S teleseismic receiver function technique to determine the Moho depth.

To derive the structural response (receiver functions) beneath the recording station, the source-equalization method (Langston, 1979) was generally applied for the coda part of teleseismic P-waves.

In general, the receiver functions sample the structure over a range of tens of kilometers from the station in the direction of wave approach. The specific sample width depends on the depth of the deepest contrast(Nasrabadi, 2008). Recent innovations in receiver function analysis include more detailed modeling of receiver function arrivals from sedimentary basin structures (e.g. Clitheroe et al., 2000), anisotropic structures (e.g. Levin and Park, 1997), and estimation of Poissons ratio (e.g., Zandt and Ammon, 1995; Zhu and Kanamori, 2000). In deconvolving the radial component from vertical a wave form whose peaks indicate velocity contrast beneath the seismometer will be found. The deconvolution result in turn shows the geology and structure beneath and near the receiver and due to this it is named as receiver function.

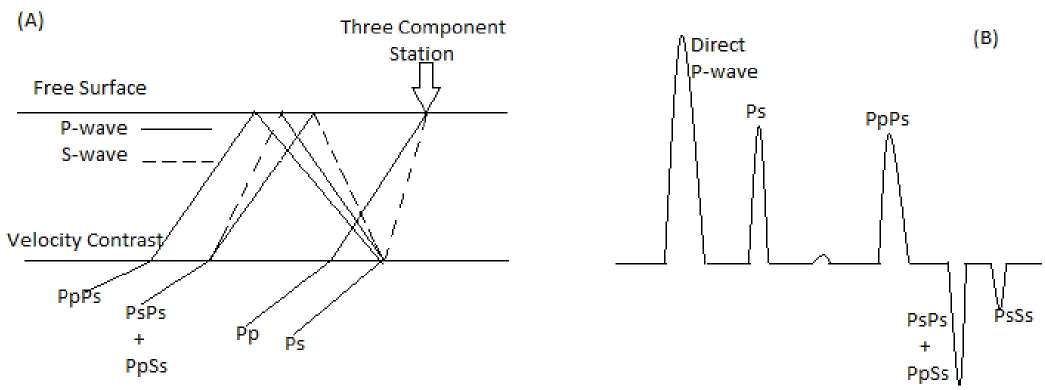

Figure 3.1: (A) is a graphical representation of receiver functions and (B) is a receiver function that shows the direct P-wave and the reverberations (Ps, PpPs, PsPs + PpSs).

At any subhorizontal interface with sufficient impedance contrasts, a portion of the subvertical P-wave energy converts to a Ps phase (Figure 3.1). The receiver function is the transfer function between the P wave with all associated P multiples and reverberations and the Ps phases with their multiples and reverberations (Figure. 3.2) (Ammon, 1991; Jesse, 2004). P- to -S conversions caused by any interface with a significant acoustic impedance contrast occur as peaks on RFs, at times related to their depth beneath the recording seismic station. Vertically polarized converted S waves dominate the radial component of a RF (R) whereas horizontally polarized converted S waves dominate the transverse component (T). Radial component seismograms record P-to-S conversions and multiple reverberations shortly after the initial P waves (Burdick and Langston, 1977; Jesse, 2004).

3.1.1 Rotation of Data

Before the beginning of the data analysis from teleseismic events we used tapering which is necessary to reduce spectral artifacts by applying a window to the data to acquire better P-onset arrival time. Inaddition to tapering, rotating coordinate from ZNE(Z = vertical, N = north, E = east) to ZRT(Z = vertical, R = radial, T = transversal) was depleted by using back azimuth and appling the following mathematical steps. The importance of this rotation is to isolate the converted S phase from direct P wave as Z component is invarient during rotation as shown below.

$$E_R = E_E cos\theta + E_N sin\theta \tag{3.1}$$

$$E_T = -E_E sin\theta + E_N cos\theta \tag{3.2}$$

$$E_Z = E_Z \tag{3.3}$$

Where, E implies the impulse response of the earth's structure, $\theta = 270 - \gamma$ and γ is the back azimuth. The back azimuth describes the angle between the vector pointing from the seismic station to the north.

In this work we use an earthquake of 5.5 magnitude with a better P-wave having high signal to noise ratio and epicentral distance of 30^o to 100^o(1^o = 111.11 km). Three components (Z, R, T) of the total response at a station on a teleseismic P wave can mathematically expressed as:

$$D_R(t) = I(t) * S(t) * E_R(t) \tag{3.4}$$

$$D_T(t) = I(t) * S(t) * E_T(t) \tag{3.5}$$

$$D_Z(t) = I(t) * S(t) * E_Z(t) \tag{3.6}$$

where $I(t)$ is impulse response of the seismogram, $S(t)$ is the effective seismic source function, and $E(t)$ implies the impulse response of the earth's structure in time domain(Langston, 1979). Therefore, the very target of this method is to find the value of impulse response of the earth's structure. In the source equalization method, for a steeply incident P wave the value of impulse response of the earth's structure in the vertical direction(perpendicular component) is assumed to be equal to dirac-delta function(Langston, 1979).

$$E_z(t) = \delta(t) \tag{3.7}$$

Where, $\delta(t)$ is Dirac delta function but $E_R(t)$ and $E_T(t)$ are observed structual response. We found the radial and tangential component of observed structural response by deconvolving the vertical component from the radial and tangential component of the response to remove the signature of the source and instrument responses from the waveforms (Langston, 1979). Using equation (3.6) and (3.7), The vertical component of the impulse response can take the form,

$$D_z(t) = I(t) * S(t) \tag{3.8}$$

3.2 Deconvolution and Gaussian Filter for RFs

For earthquakes at epicentral distance more than 30^o, P waves are steeply incident and dominate the vertical component, whereas converted phase Ps are contained on the horizontal components of ground motion. The amplitude and time of the arrivals in a receiver function depends on the incidence angle of the impinging P wave and the size of the velocity contrasts generating the conversion (Ps) and multiples (PpPs, PpSs etc).

The radial receiver function is a record of radial ground phases on the radial

receiver function being attributed to motion from a near vertical incidence teleseismic P wave and is vertical structure do not have corresponding phases of computed by deconvolving the vertical component from the tangential ground motion that are large. This can easily be radial component of the P wave coda [e.g., Langston, 1979; Owens et al., 1988]. To find the moho depth, crust(Upper and lower crust) and upper most mantle, it is good to know coda value of teleseismic P-waves. The instrument response and the gains corrected before proceeding to the receiver function deconvolution.
There are two kinds of deconvolution to determine seismic wave velocity structures of crust and upper mantle beneath seismic station these are:

1. Employing a deconvolution filltering which is directly accomplished in time domain (Vinnik, 1977)
2. Employing in source equalization process which is performed by spectral division in frequency domain(SDD) (Langston, 1977).

We have employed the second method by removing source and deep mantle effects from teleseismograms. In SDD technique the response of $E_z(t)$ and $E_R(t)$ must be transformed to $E_z(\omega)$ and $E_R(\omega)$ using Fourier Transformation, then it will be simple for division. It is possible to convert arrival time of converted (Ps) wave phases to depth whenever the traveling seismic wave reaches. Water-Level Deconvolution technique Modelling and inversion to generate receiver functions has been a powerful technique in the study of crustal and upper mantle discontinuities. RF is a time series deconvolving vertical components of teleseismic body wave from the horizontal ones. This deconvolution process removes the source time functions and the effect of instruments from the waveform, thereby isolating converted waves (Ammon, 1991). In studies of the deep crust, receiver functions are usually used for frequencies below about 1 Hz with a low-pass Gaussian filter commonly applied during the deconvolution process. This is due to the high frequencies being more susceptible to scattering from small scale lateral structure variations, as well as to the low strength of earthquake signals at frequencies above 4 Hz when recorded at long teleseismic distances (e.g., Ammon et al., 1990). In deconvolving the radial component from vertical a wave form whose peaks indicate positive or negative velocity contrast can be found. The recorded seismic waveform of a distant earthquake includes information about the source, path through the mantle and local structure under the station. The recorded traces Z (vertical component) and R (horizontalradial component) of a P-wave train can be expressed in the frequency domain as:

$$D_Z(\omega) = S(\omega).E_z(\omega).I(\omega) \tag{3.9}$$

$$D_R(\omega) = S(\omega).E_R(\omega).I(\omega) \tag{3.10}$$

$$D_T(\omega) = S(\omega).E_T(\omega).I(\omega) \tag{3.11}$$

where, $S(\omega)$ is the source signature of the P-wave signal incident beneath the layers near the station; $E_Z(\omega)$, $E_R(\omega)$ and $E_T(\omega)$ are the vertical radial and tangential component response of the earth structure respectively and similarly $I(\omega)$ is the instrumental response in frequency domain (Langston, 1979; Ammon, 1991 and Zevallos, 2009).

The values $D_z(\omega)$, $D_R(\omega)$, and $D_T(\omega)$ are the Fourier Transform of $D_z(t)$, $D_R(t)$, and $D_T(t)$ respectively. One can simplify the above equations by simple division to calculate the radial and tangential receiver function:

$$RF_R(\omega) = \frac{I(\omega)S(\omega)E_R(\omega)}{I(\omega)S(\omega)E_z(\omega)} = \frac{D_R(\omega)}{D_z(\omega)} \tag{3.12}$$

$$RF_T(\omega) = \frac{I(\omega)S(\omega)E_T(\omega)}{I(\omega)S(\omega)E_z(\omega)} = \frac{D_T(\omega)}{D_z(\omega)} \tag{3.13}$$

As stated above according to Langston et al. 1979 the vertical component of ground motion for a steeply incident P wave consists of a large direct arrival followed by only minor arrivals due to crustal reverberations and phase conversions. Due to this, he asumed that $E_z(t) = \delta(t)$, where $\delta(t)$ is the Dirac delta function and named as the source equalization approach.

The Mathematical conclusion (Langston, 1979) is the radial receiver function is approximately equal to the radial impulse response of the Earth structure and in similar manner the tangential receiver function equal to the tangential impulse response of the Earth structure. This applies mathematically as follow to the seismogram with a high signal to noise ratio:

$$RF_R(\omega) \approx E_R(\omega) \tag{3.14}$$

$$RF_T(\omega) \approx E_T(\omega) \tag{3.15}$$

Equation(3.13) can be written by introducing minimum allowable amplitude level, the waterlevel, for the amplitude spectrum of the vertical component. The water level stabilizes the deconvolution by reducing magnitude of the trough in the vertical component spectrum to avoid division by very small numbers. This can be written as:

$$RF_R(\omega) = \frac{D_R(\omega)D_z^*(\omega)}{D_z(\omega)D_z^*(\omega)} = \frac{D_R(\omega)D_z^*(\omega)}{\Phi(\omega)}G(\omega) \tag{3.16}$$

Where, $D_z(\omega)$ and $D_R(\omega)$ are the vertical and radial components of ground motion in the frequency domain respectively, $*$ indicates the complex conjugate. To exclude high frequency noise from the final inversion results we have estimated the value of smoothness parameter with a Gaussian function.

High-frequencies are excluded by using a Gaussian filter, we set the parameter a of the Gaussian filter to 1.00, which gives an effective high-frequency limit of about 0.5 Hz in the P-wave data. Useful teleseismic waves have frequencies in the range of $0.1Hz$ to $1.0Hz$. At most stations, the structure varies with azimuth and even in the simplest cases, the response can vary with distance from the station.

We group the observations by azimuth and distance. For deep crustal studies with RF, frequencies lower than about 1 Hz are commonly used. Much higher frequencies are necessary to study shallow layers. This is based on the assumption that the main interfaces, such as lower mantle and Upper mantle, should have large contrasts in seismic velocity.
For a steeply incident wave beneath a homogeneous, horizontally layered structure, all multiply reflected and conversions that arrive at the station as a P wave will have the vertical and horizontal components with the same amplitude ratio. For this reason, in the deconvolution process all smaller secondary P arrivals are cancelled and the only P-wave is the "direct" arrival (Ammon, 1991). In other words, multiple P-wave arrivals from reverberations Ps, PsPmP + PpSmP and PsSmP (P, p-longitudal, S, s-shear waves, m-reflection from the Moho) within the structure cannot be distinguished easily from a source signature with several pulses, and so are removed in the deconvolution. Several methods are available to deconvolve the vertical from the radial component. The most commonly used is simple spectral division of the radial and vertical FFT components to give:

$$RF_R(\omega) = \frac{D_R(\omega)D_z^*(\omega)}{\Phi(\omega)}G(\omega) \tag{3.17}$$

where $G(\omega)$ is a low-pass Gaussian filter to select the appropriate and fittest frequency range of interest. Therefore, the above equation could take the most commonly used simple spectral division form of the radial and vertical Fast Fourier transform(FFT) components:

$$RF_R(\omega) = \frac{D_R(\omega)D_z^*(\omega)}{\Phi(\omega)}exp\{\frac{-\omega^2}{4a^2}\} \tag{3.18}$$

where, $\Phi(\omega) = max[D_z(\omega)D_z^*(\omega), C.max\{D_z(\omega)D_z^*(\omega)\}]$, C is the water level parameter used to avoid division instabilities at spectral holes of the vertical component (Ammon, 1990), $D_z^*(\omega)$ is the complex conjugate of $D_z(\omega)$ and $RF_R(\omega)$ is the radial receiver function in the frequency domain. In this work water-level constant and the Gaussian width, a are used. In the frequency domain deconvolution, the receiver function $RF_R(\omega)$ is obtained by deconvolving the vertical component $D_z(\omega)$ of an earthquake recording, from the radial component $D_R(\omega)$. C is the water level parameter and a is the width factor for the Gaussian filter to control the width of the Gaussian pulse.

The Gaussian width factor a is approximately chosen to exclude the high frequency noise introduced during deconvolution or limit the effect of high frequency scattered energy. High values of a were found to give noisy receiver functions. The level of scattering in such receiver functions would be enough to lead to potentially biased inversion results (Midzi, 2001; Mangino et al., 1993). The water-level constant limits the value of the denominator to avoid dividing by zero(Clayton and Wiggins, 1976; Mangino et al., 1993). If $C = 0$, the deconvolution is the best estimate of the true impulse response to give best arrival time resolution and $C = 1$, the deconvolution represents the least-square estimate of the true arrival amplitude. The value of C is selected as small as possible for a better resolution of arrival times. The deconvolution is performed for every event over a range of C values (1.0 to 0.0001) and the judgment is made based on the result(Ammon, 1991; Cassidy, 1992 and Midzi, 2001).

The receiver function from a smaller value of the Gaussian width tends to smooth over the effects of small-scale crustal heterogeneities and produce simpler structures with layer thickness resolutions equal to or greater than 7 km (Midzi, 2001).

3.3 Inversion of receiver functions

3.3.1 Linearized inversion

Modelling the receiver function waveform is a highly non-unique problem because any specific peak can be interpreted in different ways, such as a P to S conversion from a deep interface or a multiply reflected phase from a shallower layer. Linearization methods can be used to model RF (Ammon et al., 1990) using several different starting models chosen randomly to account for the nonuniqueness. Regularization is often necessary, such as smoothness constraints, to stabilize the solutions. A linearized inversion is a kind of stacking certain receiver functions calculated by the time-domain deconvolution. Because of the non-uniqueness problem the final solution depends strongly on the initial model. To constraint an absolute velocity to get depth to moho is by adding a priori information(Ammon et al. 1990). Densities are calculated either by velocity density relations or impedance contrast from the overlying layer and not independently varied (Lodge et al. 2009).

This study begins with a simple forward modelling exercise to build an initial velocity-depth model. Initially, a twenty layer velocity model is chosen, to arrive at the final synthetic seismogram after many iterations. This is done by taking the fittest model as an initial velocity-depth model for the second action to come up to the final and most fittest synthetic seismogram with the observed wave-form by putting all of the arrivals in the first 25 s after the direct P arrival. The waveform contains the information on the shallow crustal and upper mantle structure, which is of particular interest.

3.3.2 Inversion of RFs by genetic algorithm

Genetic Algorithm (GA) is a method to select the best models from a population of randomly chosen tentative models, based on "survival of the fittest" criteria (Zevallos, 2009 and referenced therein). The best models from one generation (population) are combined (mated) with cross-over operations to produce offspring models which will take part in a new, better fitting generation of models. The basis for using genetic mechanisms is that the cross-over operation has a good probability of combining the good genes (model parameters) from each parent and produce an offspring with a better fitting than any of its parents. Mutation operations, where one or more genes (model parameters) are randomly altered, are also important as they ensure population diversity and help avoid the population of models evolve towards a local minimum in fitting the data (Zevallos, 2009).

3.4 Evaluation of Moho Depth(H) and $\frac{V_P}{V_S}$ Ratio

For a P-wave with a vertical incidence converted to an S-wave at a depth H, one can estimate the depth at which they were produced using basic mathematical formulas and algorithms starting from the following ray-diagrams:

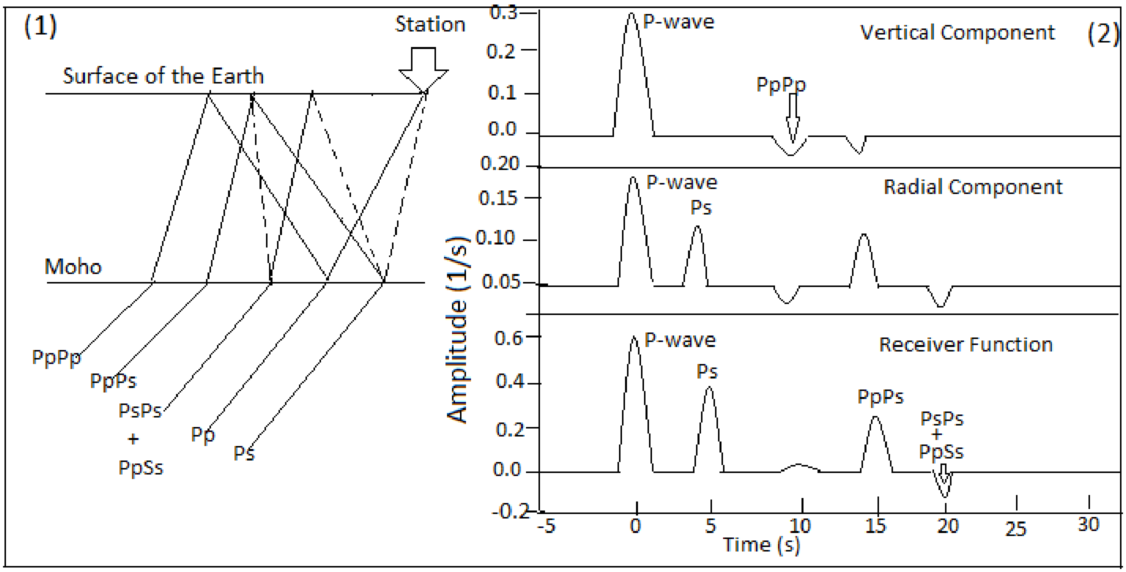

Figure 3.2: (1) Simplified ray diagram identifying the major P-to-S converted phases, which comprise the receiver function for a single layer over a half-space. (2) Vertical and radial synthetic seismograms and the corresponding receiver function calculated for a single layer.

To estimate the Moho depth beneath the seismometer, let us evaluate the value of average velocity by applying kinematic equation for one particle by applying seismic anisotropy concept

$$t_{Ps} - t_P = \frac{H}{V_s} - \frac{H}{V_P} = H\left(\frac{1}{V_s} - \frac{1}{V_P}\right) \tag{3.19}$$

$$t_{PpPs} - t_P = \frac{H}{V_P} + \frac{H}{V_P} + \frac{H}{V_s} - \frac{H}{V_P} = H\left(\frac{1}{V_s} + \frac{1}{V_P}\right) \tag{3.20}$$

$$H = (t_{Ps} - t_p)\left\{\frac{V_p V_s}{V_p - V_s}\right\} \tag{3.21}$$

where, V_p and V_s are average velocities of P- and S-wave respectively, whereas $t_{Ps} - t_p$ is the time differece between the arrival of the direct P-wave and the converted P_s phase. This equation is purely hypothetical for horizontal discontinuities, as perpendicular rays do not undergo phase conversion. In reality, since the waves that reach the seismic station are not vertical a correction must be made for their angle of incidence. In this study we have not yet taken seismic anisotropy by assuming that seismic waves have the same velocity in all directions, then the above equation becomes (e.g. Sheriff and Geldart, 1982; Stankiewicz, 2002):

$$H = \frac{t_{Ps} - t_p}{\left[\left(\frac{1-p^2V_s^2}{V_s^2}\right)^{1/2} - \left(\frac{1-p^2V_p^2}{V_p^2}\right)^{1/2}\right]} = \frac{t_{Ps} - t_p}{\Phi_s - \Phi_p} \tag{3.22}$$

$$H = \frac{t_{PpPs} - t_p}{\left[\left(\frac{1-p^2V_s^2}{V_s^2}\right)^{1/2} + \left(\frac{1-p^2V_p^2}{V_p^2}\right)^{1/2}\right]} = \frac{t_{Ps} - t_p}{\Phi_s - \Phi_p} \tag{3.23}$$

where, $\Phi_s = \sqrt{V_s^{-2} - p^2}$ and $\Phi_p = \sqrt{V_p^{-2} - p^2}$are the vertical slownesses of the S- and P-waves, respectively. p is the ray parameter in $\frac{S}{km}$ but V_s and V_p, are the average crustal shear and compression wave velocities, respectively.

Poissons ratio is a quantity related to the elasticity of a medium. It is defined as the ratio of lateral contraction to the longitudinal extension of the body when it is placed under stress (Bullen and Bolt, 1947). For an isotropic medium it can be expressed in terms of the two Lam elastic parameters, λ and μ (the rigidity, or shear modulus):

$$\sigma = \frac{1}{2}\left(\frac{\lambda}{\lambda + \mu}\right) \tag{3.24}$$

$$\Lambda + 1 = \frac{1}{2\sigma}\Lambda \tag{3.25}$$

For a perfectly elastic solid(Poissons medium) $\Lambda = 1$, then the value of σ is 0.25. Similarly, if $\mu = 0$ then the value of σ is 0.5 for a perfect fluid.
According to Bullen and Bolt et al. 1947 the ratio of the primary longitudinal wave velocity to that of the secondary transverse wave

$$\left(\frac{V_p}{V_s}\right)^2 = \left(\frac{\lambda + 2\mu}{\mu}\right) \tag{3.26}$$

$$\Lambda + 2 = \left(\frac{V_p}{V_s}\right)^2 \tag{3.27}$$

where $\frac{\lambda}{\mu} = \Lambda$.
When eqn (3.24) and eqn (3.26) are simultaneously solved the value of Λ is:

$$\Lambda = \left[\left(\frac{V_p}{V_s}\right)^2 - 1\right]\frac{\sigma}{0.5} \tag{3.28}$$

By substituting eqn (3.27) in eqn (3.24) and rearranging gives us the value of poissons ratio as:

$$\sigma = 0.5\left[1 - \frac{1}{\left(\frac{V_p}{V_s}\right)^2 - 1}\right] \tag{3.29}$$

Moho depth and poissons ratio can be evaluated using travel times $t_{Ps} - t_P$ and

$t_{PpPs} - t_P$ [Zandt et al. (1995)]. These values can be equated from equation (3.21) and (3.22) and gives:

$$t_{Ps} - t_p = \frac{H}{V_P}\left\{\left[\sqrt{\left(\frac{V_p}{V_s}\right)^2 - P^2V_P^2}\right] - \left[\sqrt{1 - P^2V_P^2}\right]\right\} \tag{3.30}$$

and

$$t_{PpPs} - t_p = \frac{H}{V_P}\left\{\left[\sqrt{\left(\frac{V_p}{V_s}\right)^2 - P^2V_P^2}\right] + \left[\sqrt{1 - P^2V_P^2}\right]\right\} \tag{3.31}$$

As shown in the above equations the travel times depend on three crustal parameters: the P-wave velocity, the $\frac{V_p}{Vs}$ ratio, and the crustal thickness H. To find the value of H using the above equation V_s and V_p must be known. If V_s is assumed, V_p, can be found from the time interval between the arrival of the Moho Ps converted phase and the Moho $PpPs$ phase $t_{PpPs} - t_{Ps}$ by solving

$$\frac{V_p}{V_s} = \sqrt{\left(1 - P^2V_P^2\right)\left[1 + 2\left(\frac{t_{Ps} - t_p}{t_{PpPs} - t_p}\right)\right] + P^2V_P^2} \tag{3.32}$$

By assuming V_s it is possible to obtain Moho depth and Poisson's ratio for the crust. The estimate of Poisson's ratio is only slightly dependent upon the value chosen for V_s, (i.e., it changes at most by 0.01 over a 0.3 $\frac{km}{s}$ change in V_s)(Last, 1997). Christensen and Mooney et al. (1995) calculated a mean crustal compressional velocity of 6.45 $\frac{km}{s}$ from laboratory measurements of the velocities of dierent crustal rocks and their relative global abundance. We determined the ray parameter P from the event depth and epicentral distance and use average crustal P-wave velocities of 6.2 and 6.4 km/s (Li and Mooney, 1998)

3.5 Inversion of RFs to Model Moho-Depth vs V_P

Information of crustal structure under a station derived from the radial receiver function which is dominated by seismic P- to S-wave convertion from a series of velocity discontinuities in the crust and upper mantle. Because of the large velocity contrast at the crust-mantle boundary (Moho-depth) at which P-to S-wave conversion is occured. By using the time difference between the reververation time (t_{Ps} and t_{PpPs}) and direct P arrival time (t_{Ps}) can be used to estimate crustal thickness by assuming the average crustal velocities and ray-parameter.

$$H = \frac{t_{Ps} - t_p}{\sqrt{\frac{1}{V_s^2} - P^2} - \sqrt{\frac{1}{V_p^2} - P^2}} \tag{3.33}$$

and

$$H = \frac{t_{PpPs} - t_p}{\sqrt{\frac{1}{V_s^2} - P^2} + \sqrt{\frac{1}{V_p^2} - P^2}} \tag{3.34}$$

These equations relate the time diffrences $t_{Ps} - t_p$ and $t_{PpPs} - t_p$ to the depth at which the conversion took place, H, where V_P and V_S are the average P- and S-wave velocities above the depth of the conversion and p is the ray parameter (Zhu and Kanamori, 2000).

CHAPTER 4

DATA COLLECTION AND ANALYSIS

In this study, teleseismic data from four broadband seismological stations were collected. The stations are Ankober, Semera, Harar and Dila. We used a global earthquake catalogue from the International Earthquake Information Center to extract teleseismic events with magnitudes larger than 5.5 and epicentral distance between 30^o and 100^o for the RF analysis.

The collected data for three years in the Institute of Geophysics Space Science and Astronomy(IGSSA) were used for RFs analysis. The selection criteria of events at each station depends on the signal-to-noise ratio.

First step of RF processing was original components of seismogram (Z, N, E) rotated into vertical, radial, and tangential (Z, R, T) components or into ray-parameter coordinate system (L, Q, T) which is useful to separate different wave types P, SV, and SH. In the estimation of the Moho depth, the delay time of P-to-S converted waves is compared to the direct P-wave (e.g., Langston 1979; Ammon 1991). To investigate one dimensional seismic wave velocity structure beneath the station the time-domain inversion methods of Ammon et al. 1990 were applied to the radial receiver function.

In order to characterize crustal structure in the four stations, the technique applied was frequency domain deconvolution RFs (Langston, 1977). Certain signal correction operations have been applied to remove the mean from data using Seismic Analysis Code (SAC) software by using the command rmean to the desired spectrum by subtracting the mean from all the points and compute the Fourier transform or power spectrum of the tapered signal. When frequency content of a signal is computed errors may arise due to a limited-duration snapshot of a signal that actually lasts for a longer time. Windowing is a way to reduce these errors, though it cannot eliminate them completely. The discontinuity and the resulting spurious high frequencies have been suppressed in the frequency analysis, by tapering the recorded signal smoothly to zero at the start and end of the recording period. Then, the data is deconvolved to radial and tangential components before the stacking processes was done. Finaly, the stacked radial receiver function is interpolated to DELTA 0.0250 and number of points(NPTS) 350, which minimizes the value of NPTS of stacked RFs from ~ 3800. This was one of the important steps before inversion is done to deduce bulk crustal properties (crustal thickness (H) and $\frac{Vp}{Vs}$ ratio.

4.1 Inverse Methods for Receiver Functions Analysis

By applying the computational approach of Ammon et al. 1990 and 1991 which is the processes of deconvolving the vertical from radial and transverse components to get radial and transverse receiver functions. Using the direct P-to-S conversion time t1, there is a trade off between the determination of H and $\frac{Vp}{Vs}$ (Ammon, 1990). Consider the arrival time of P, Ps, PpPs, and PpSs + PsPs to be t1, t2, and t3 respectively. By using the direct P-to-S conversion it is possible to calculate the value of H, depth to the Moho and $\frac{Vp}{Vs}$. These two values can also be found using the times of arrivals of the reverberations (Zhu and Kanamori et al. 2000). The arrival-times of the three arrivals (t1 ,t2 ,t3) relative to the direct P-wave are calculated and analysed by using Receiver function code prepared by Chuck Ammon 1991. The deconvolution was done in the frequency domain using the water-level method (Clayton and Wiggins, 1976). The results of the inversion are non-unique and dependent on the starting model (Ammon et al., 1990). Therefore, we carefully built our initial model by considering the previous work conducted in and around the study areas.

4.2 Data acquisition

The data in this study were collected from september 2014 to august 2015 by Institute of geophysics Space Science and Astronomy (IGSSA), Addis Ababa University. The station used in this work are permanent and named as Ankober(ANKE), Semera (SEME), Harar (HARE) and Dila (DILA). First, the selected teleseismic wave form data traces were windowed by applying a cosine tapered boxcar window from 10 s before to 25 s after the direct P-wave arrival to deconvolve the vertical component from the radial component to remove the signature of the source and instrument responses from the waveforms (Langston 1979).

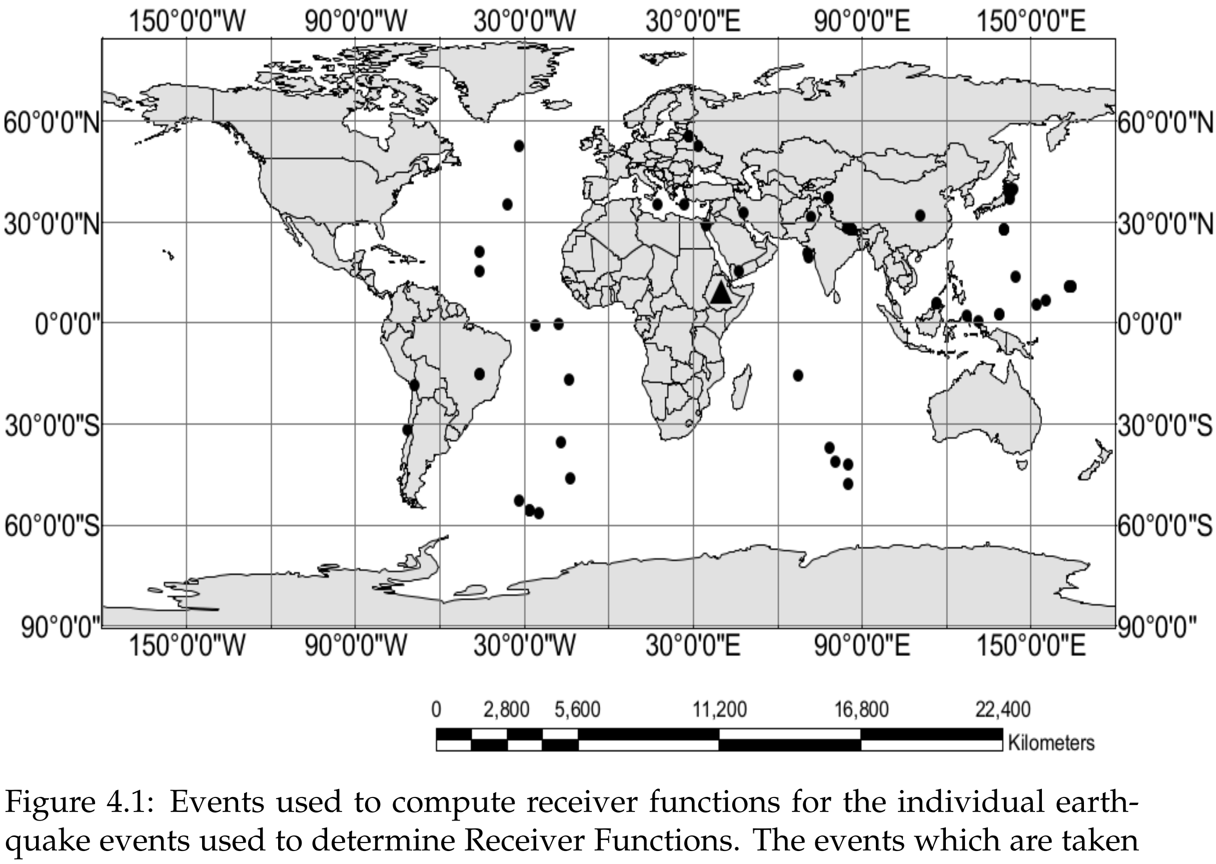

Figure 4.1: Events used to compute receiver functions for the individual earthquake events used to determine Receiver Functions. The events which are taken from these earthquakes are those with magnitude greater than 5.5mb and having epicentral distances from 30^o to 100^o between the earthquake sources and the permanent seismic stations located in ethiopia (black triangle).

The collected teleseismic data were classified in to four groups for analysis according to the direction they emanated from. The classifications of these data were by checking the azimuthal dependence of the waveforms. The results were investigated by plotting the individual deconvolved traces against the station backazimuth, and no significant variations were detected. The teleseismic sources are mainly located north east, south east and south west off the stations. Transverse receiver functions, which are the results of deconvolving the vertical traces from the corresponding transverse traces, were also obtained to assess the potential signature of anisotropy and heterogeneity from the underlying structures, and no significant transverse amplitudes were observed at any station. It was, therefore, assumed that isotropic, laterally homogeneous layered structures beneath the stations would suffice to explain the main features in the receiver function waveforms. The data from three different azimuthal directions (by neglecting wave forms coming from North west direction, having bad signal to noise ratio) treated independently and did not give a significantly different result from the stacked result. Therefore, this work analyzes the stacked result of each stations from different directions.

4.3 Data Processing

4.3.1 Data Selection Principles

1. Teleseismic events with epicentral distance of 30^o to 100^o were selected to calculate receiver function. For measurements closer than 30^o, the P-wave of the waveform is complicated by upper mantle travel path effects. On the other hand, if it is farther than 100^o, the station is located within the shadow zone of the direct P-wave. Due to this factor, we haven't yet used the teleseismic wave form data whose azimuthal coverage is not in the limit between 30^o to 100^o

2. The magnitude of the teleseismic earthquakes recorded in the stations was above 5.5 as smaller magnitudes didn't show clear peaks and troughs in the

waveforms.

3. These earthquakes were with different hypocenteral depth(an earthquake location where the fault rupture starts).

4. Different number of earthquake events were used in four stations i.e 39 for SEME, 20 for ANKE, 16 for DILA and 14 for HARE. Even if the number of events are limited but with good data quality.

4.3.2 Pre-Processing

Teleseismic earthquake events (see Figure 4.1) having epicentral distance ranging from 30^o to 100^o were selected. The data-set used for this study for different stations were diverse in numbers (e.g 39 and 20 teleseismic events were taken for Semera(SEME)and Ankober(ANKE) respectively) depending on the signal to noise ratio of the seismic wave-form data. These seismic stations are parts of the IGSSA Seismic broad band Network Stations, which are controled by Addis Ababa University.
After the data were choosen by using SEISAN and PQL softwares, those data which were in the fittest epicentral distance range with better signal to noise ratio have been converted to SAC format.

4.3.3 Main-Processing

The pre-processing task including data quality check, reading of P onset, tapering, rotation and cutting of data was done using the SAC software (Goldstein, 1999). The deconvolution and inversion of receiver functions was done using the programs prepared by Ammon and others (Ammon, 1991 and referenced therein). Receiver functions were calculated for every event using a water level constant of $c = 0.001$ and a Gaussian filter constant of a used is either 1.0, 1.5, or

2.5. To get a better signal to noise ratio the number of events are stacked. The stacked receiver functions were then inverted to obtain the plane layered crustal velocity structure. Due to the non-uniqueness of the problem (Ammon et al., 1990), several starting models were used for each receiver, ranging from ten layer models to a gradient model with 30 layers. We used the inversion using starting models with 20 and more layers. In addition synthetic forward modelling was used to refine initial models. In this work inversion of Receiver Function, a smoothness factor of $\sigma = 0.0 - 2.0$ in ″smthinv″ and $\sigma = 1.0$ in ″manyinv″ were used, which gave better RMS fit between synthetic and observed receiver functions. By allowing larger roughness we have found best fit but seem to be unrealistic solutions, this phenomenon have also been referred in the work of Ammon et al., 1991. But, to remove the non-uniqueness problem from each individual inversion, we minimized roughnesses constraints. A singular-value decomposition method was used to compute the matrix inverse and solve the inversion problem. The applied value of singular value truncation fraction was 0.001. There is no guarantee that a unique inversion result will be obtained, as the method seeks to minimize the differences between observed and synthetic receiver functions. We used a priori information available for the area under investigation to constrain the solutions. According to Ammon et al. 1990 when inversion technique is used the initial model must be close to the true earth velocity structure (Ammon et al., 1990).

The inversion procedure consists of preparing the observations, constructing an initial model, choosing a smoothness weight parameter, inverting the waveforms and assessing the significance of features in the results. The inversion is a search for models fitting the observations using a gradient-based inversion algorithm. The accepted solution is that which corresponds to the best fit between observed and synthetic receiver functions(Ammon, 1990).

The data was processed using a program ″pwaveqn″ that compute a source equalization deconvolution on a three component seismogram using the method of

Langston et al., 1979. The code had been written by Owens et al. 1982, modified by Randall et al. 1989 for Gaussian normalization and modified by Ammon et al. 1990 for water-level normalization. This program deconvolves the vertical component with itself using the specified water level parameter and gaussian.

4.4 Codes and Softwares Used

There are a number of programms and softwares used in this work, These are:

1. PQL (PASSCAL Quick Look)
2. SEISAN
3. SAC which is a very important software to prepare the teleseismic wave form data (Goldstein, 1999)
4. GIS
5. Rftn.Codes.Export
6. **Jinv** is a very important code that utilize a function "partials", which performs the perturbation of comperessional, shear wave velocity and density ($\frac{g}{cm^3}$) over half space by using prescribed frequency (hz) and horizontal phase slowness (p) which is about 0.06 in this work. In this subroutine dispersion due to anelasticity is also calculated.
    (a) Source Equalization (Receiver-Function Estimation) a Frequency Domain Deconvolution Program used is "pwaveqn"
    (b) Forward Modeling Program to creat a velocity model is "icmod"
    (c) Waveform Inversion Programs are:
        i. snglinv
        ii. smthinv

iii. manyinv

Overall steps done in this paper regarding the computational activities are using Fortran 77 program, especially to perform a source equalization task on a three component seismogram using the deconvolution method of Langston., 1979. This code has been written by Owens, 1982. The code implement the Gaussian normalization of Randall, 1989 and an additional water-level normalization Ammon., 1990.

The program was designed to call an assemblage of subroutines called ″subs.a″, but this conglomeration of subroutines is not available on line. Therefore, this study, by realizing the necessity of the subroutines included in subs.a, bring to bear success by calling the SAC subroutine collection tar the so called sacio.a. Using the program called ″Pwaveqn″ the deconvolution of the vertical component from itself was employed using specified water-level parameter and Gaussian width, to compute the area under the Gaussian Filter. One of the very crucial steps performed in this work was custumizing and rewriting the fortran codes, such as ″FFT″ that can apply the Fast Fourier Transform. In addition to this it was very paramount to associate the FFT and the Pwaveqn. The source equalizing software, ″Pwaveqn″ utilizes inverse transform that equalized the vertical component using ″dfftr″ which inturn used the function ″FFT (Fast-Fourier Transform)″ which we customized from 'Numerical Recipe', a book that includes number of Fortran codes (Press, 1997).

4.4.1 Data Processing using ″snglinv″

We used the ″snglinv″ Program to analyze the data. This program with additional subroutines were prepared and compiled by Ammon, 1990 and Randall, 1989. Additional routines by Zandat, 1995 and Owens, 1982. The working steps to arive at the final inversion results are:

1. Maximum number of points in each wave form was 350.
2. We generated a velocity model using ”gradmod”.
3. The max number of iterations per inversion was 4.
4. The smoothing trade-off parameter used was 2.0.
5. It required inversion ID number for output naming.
6. The Singular Value truncation fraction (water level value) used was 0.001
7. And we didn’t use high pass filter.

4.4.2 Data Processing using ”smthinv”

This is the second main program which was used to analyze the seismic waveform by smoothning the Receiver Function (Ammon, 1990; Randall, 1989; Zandat, 1995 and Owens, 1982). The working steps to arrive at the final inversion results are:

1. Maximum number of points in each wave form was 350.
2. We generated a velocity model using ”gradmod”.
3. The max number of iterations per inversion was 4.
4. The minimum smoothing trade-off parameter started in this work was from 0.0 until the maximum smoothing trade-off parameter i.e 2.0.
5. The Singular Value truncation fraction (water level value) used was 0.001
6. And we didn’t use high pass filter.

4.4.3 Data Processing using ”manyinv”

This is the last main program used in the analysis of the data to get output with many subroutines included in it. These subroutines were prepared and compiled by Ammon, 1990 and Randall, 1989. Additional routines by Zandat, 1995 and Owens, 1982. The working steps to arive at the final inversion results are:

1. Maximum number of points in each wave form was 350.
2. We generated a velocity model using ”gradmod”.
3. Maximum perturbation was $0.87\frac{km}{s}$
4. Velocity to cut purturbing off was $8.1\frac{km}{s}$
5. Maximum perturbation for random component was 20 percent of the maximum perturbation input
6. The smoothing trade-off parameter used in this work was 0.1
7. The Singular Value truncation fraction (water level value) used was 0.001
8. And we didn’t use high pass filter.

Additional activities performed in this work was the realizations of how to employ the reading or writting the SAC format teleseismic data. To do this we have to have a number of functions and subroutines that can utilize and deliver: There were some subroutines engaged to perform source equalization process. Correspondingly, there were certain steps which necessitate width of Gaussian, if the source equalization processes were consummated. Furthermore, trough filler was used during source equalization if the deconvolution process is unity (source equalized). The number of points and sampling rate in the data was very crucial in the analysis of inversion using either ”sngling”, ”smthinv” or ”manyinv”, and to do this the previous programs were designed to access ”subs.a”, which we couldn't be able to find. But, this study, by realizing the necessity of the subroutines included in ″subs.a″, bring to bear success by calling the ″SAC″ subroutine collection tar the so called ″sacio.a″.

Using ″Pwaveqn″ the deconvolution of the vertical component from itself was employed using specified water-level parameter and Gaussian width, to compute the area under the Gaussian Filter. The source equalizing software, ″Pwaveqn″ utilizes inverse transform that equalized the vertical component using ″dfftr″ which inturn used the function ″fft (Fast-Fourier Transform)″ (Press, 1997)

CHAPTER 5

RESULTS

5.1 Stacked RFs Results of Ankober Station

The figures below are stacked teleseismic receiver functions results for Ankober station to seismic waves emanating from different directions.

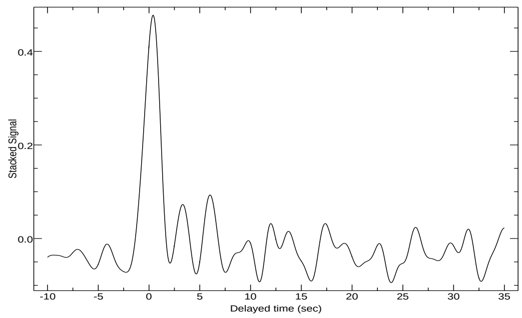

(a) Stacked of eight teleseismic events which came from north east directions to be recorded at SEME broad band stations.

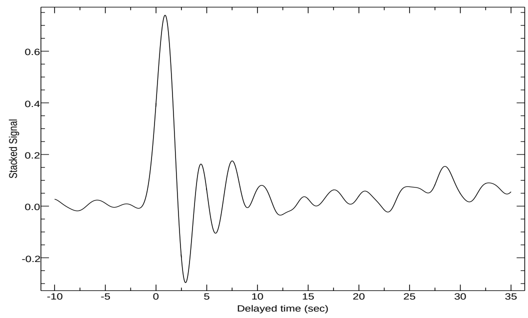

(b) Stacked of two teleseismic events which came from north west directions to be recorded at SEME broad band stations.

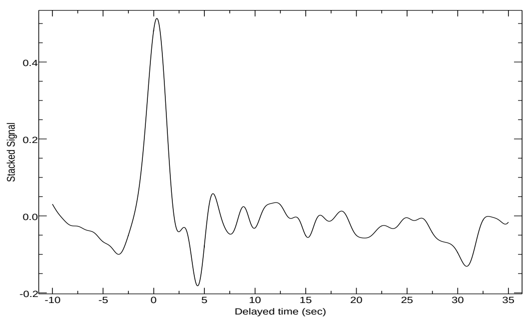

(c) Stacked of seven teleseismic events which came from south west directions to be recorded at SEME broad band stations.

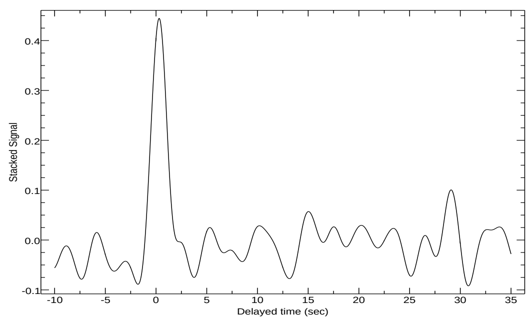

(d) Stacked of three teleseismic events which came from north east directions to be recorded at SEME broad band stations.

Figure 5.1: Stacked teleseismic events recorded at ANKE broadband station from different directions.

5.1.1 Stacked RFs Results of Semera Station

Figures below are stacked teleseismic receiver functions results for Semera station to seismic waves emanating from different directions.

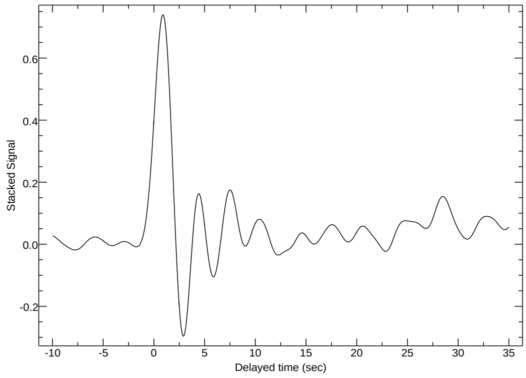

(a) Stacked of eighteen teleseismic events which came from north east directions to be recorded at SEME broad band stations.

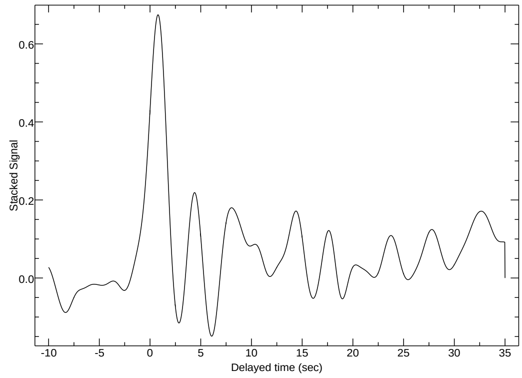

(b) Stacked of five teleseismic events which came from north west directions to be recorded at SEME broad band stations.

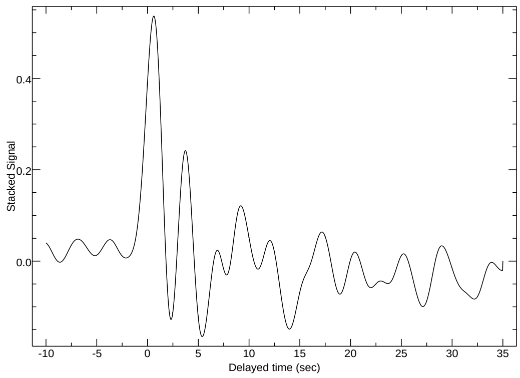

(c) Stacked of five teleseismic events which came from south west directions to be recorded at SEME broad band stations.

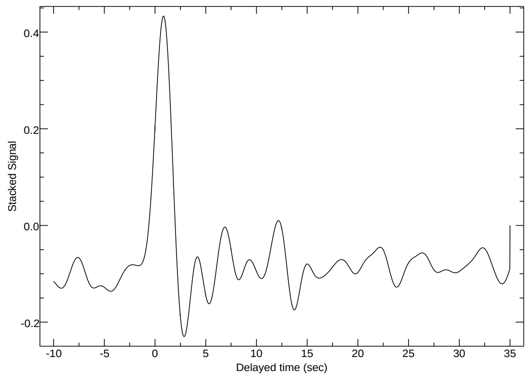

(d) Stacked of eleven teleseismic events which came from south east directions to be recorded at SEME broad band stations.

Figure 5.2: Stacked teleseismic events recorded at SEME broadband station from different directions.

5.2 Teleseismic Events Recorded in Four Ethiopian Stations

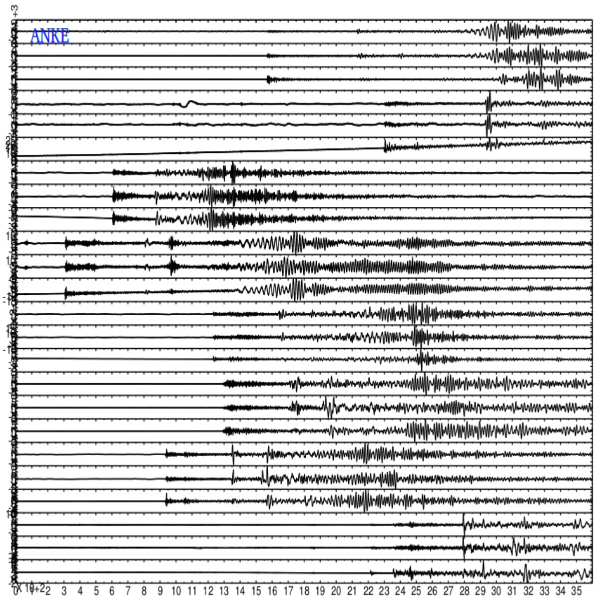

(a) Some of the teleseismic events recorded in Ankober station (ANKE) ranging from 2014 to 2015.

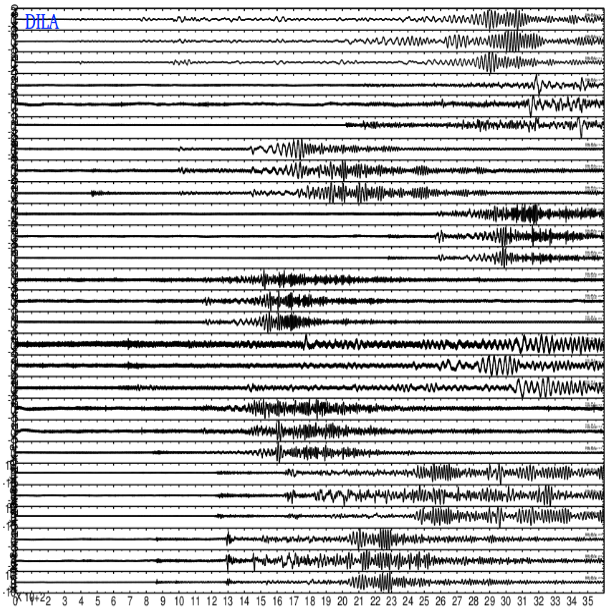

(b) Some of the teleseismic events recorded in Ankober station (DILA) ranging from 2014 to 2015.

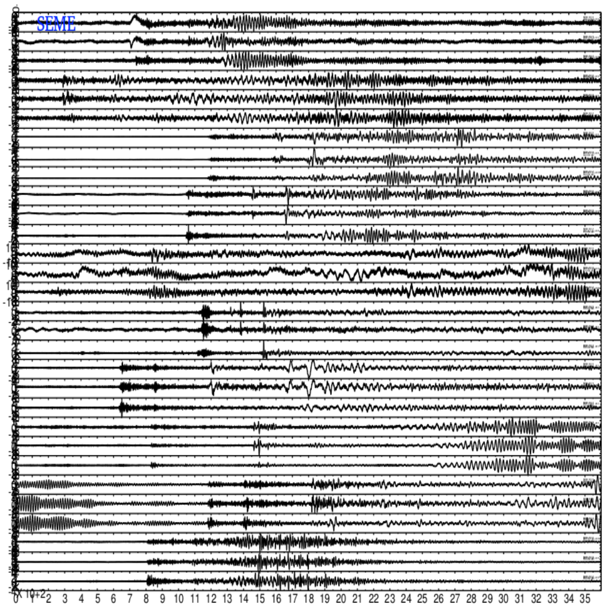

(c) Some of the teleseismic events recorded in Ankober station (SEME) ranging from 2014 to 2015.

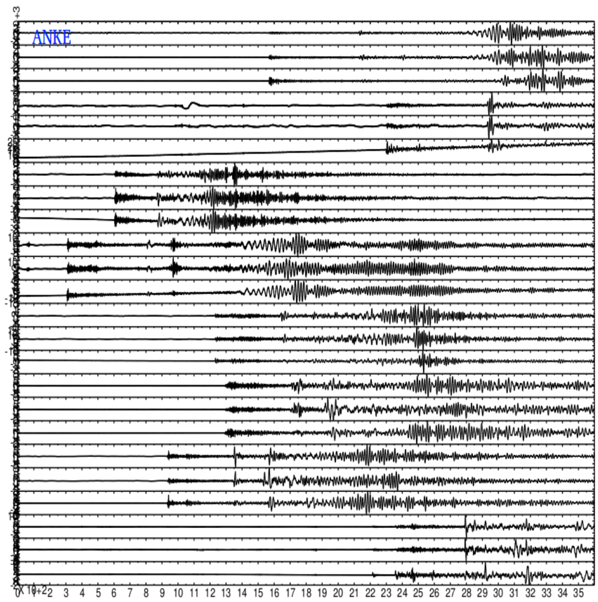

(d) Some of the teleseismic events recorded in Ankober station (HARE) ranging from 2014 to 2015.

Figure 5.3: The selected teleseismic earthquake wave form data recorded in ANKE, DILA, SEME and HARE and the stations are located in Western plateau, Southern plateau, Afar and Eastern Plateau respectively

5.3 The Source Equalization Procedure

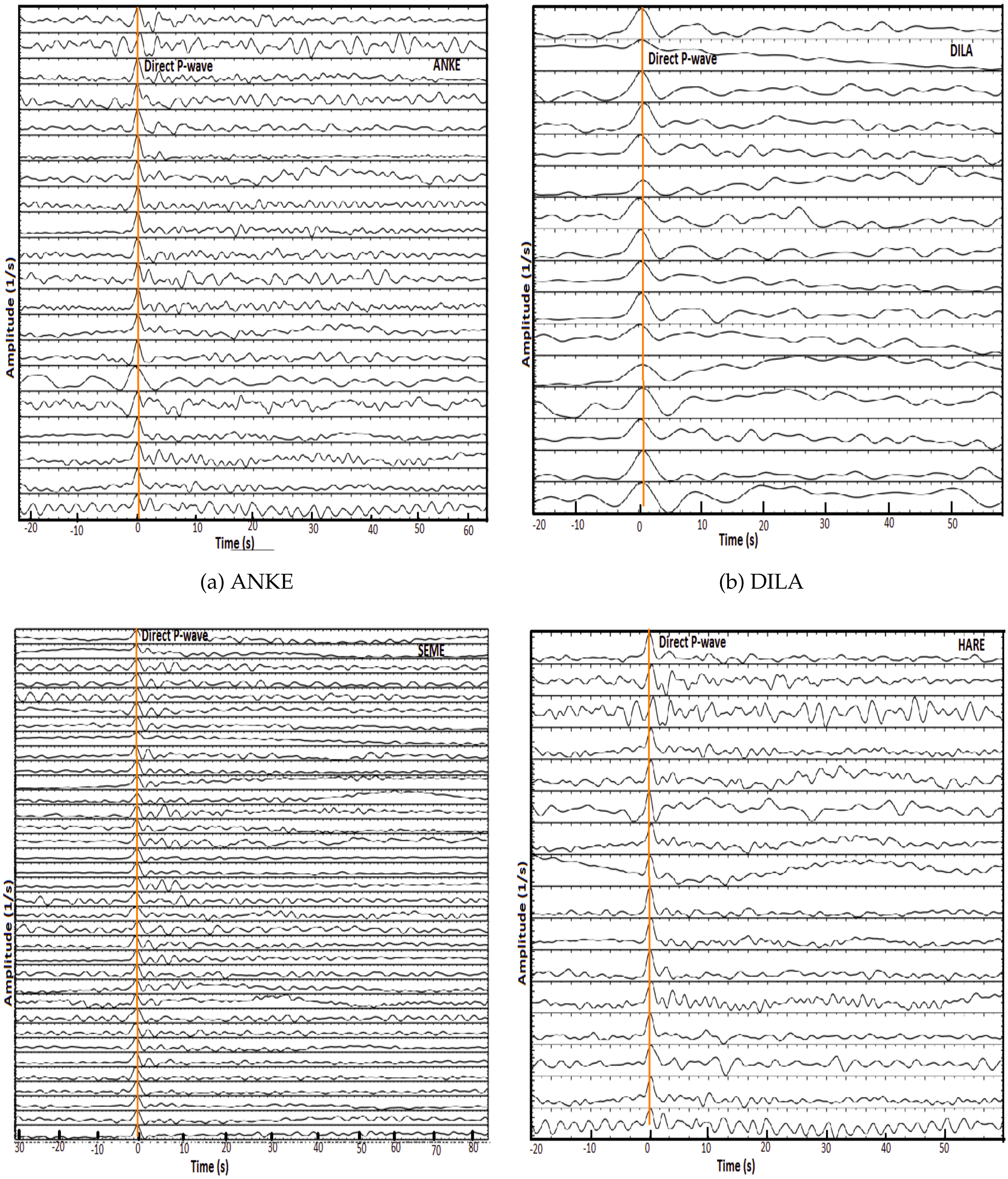

(a) ANKE

(b) DILA

(c) SEME

(d) HARE

Figure 5.4: Source equalized wave form (i.e isolating the near receiver structure from the source and distant structure such as source and propagation effects.

5.4 A stacked Receiver Function

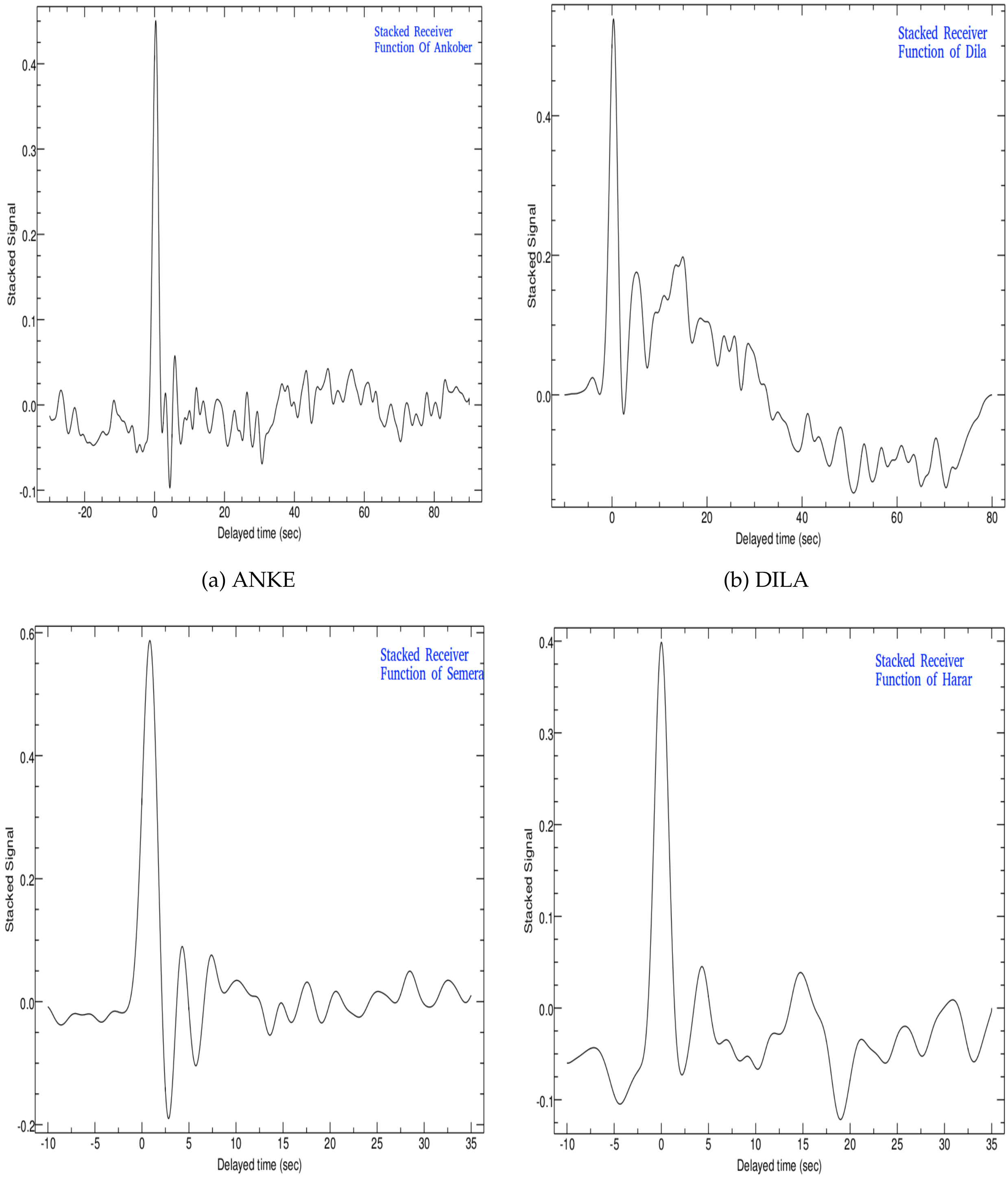

(a) ANKE

(b) DILA

(c) SEME

(d) HARE

Figure 5.5: A stacked Receiver Function plot of 20, 16, 39 and 14 teleseismic events recorded at ANKE, DILA, SEME and HARE stations respectively.

5.5 Time Shift in The Pulse

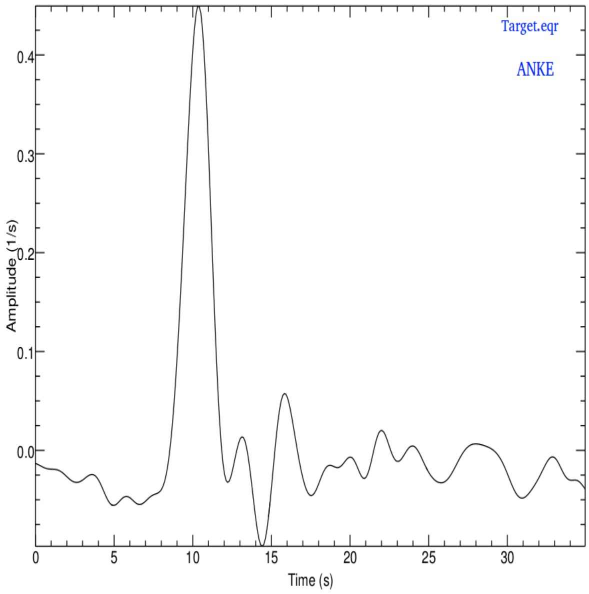

(a) ANKE

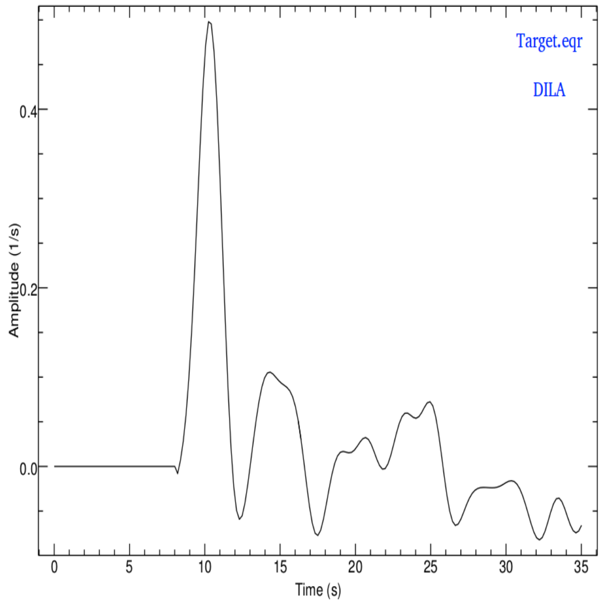

(b) DILA

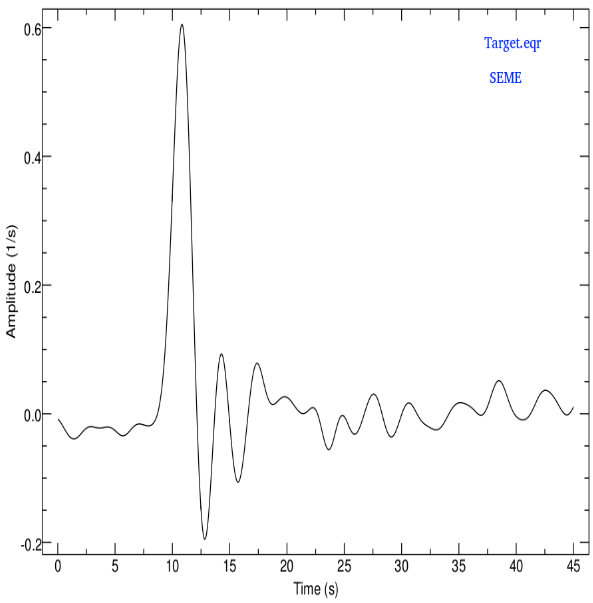

(c) SEME

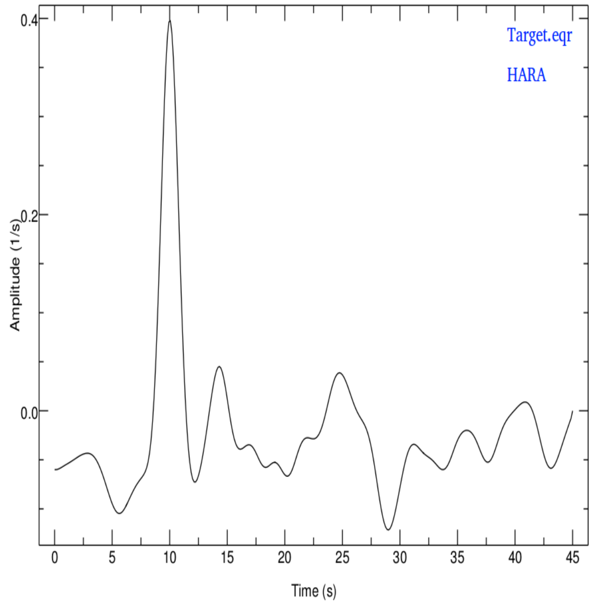

(d) HARE

Figure 5.6: A 10 second time shift in the pulse to get a clear idea of the processing noise in the resulting deconvolution. This plot is the stacked wave form between 10 to 35 seconds.

All the above steps and procedures done during stacking and source equalization processes using teleseismic events recorded at different broad band stations from three quadrant (exclusing second quadrant which is not in the range of $30^o - 100^o$).

5.6 Smoothening Model of Observed Data

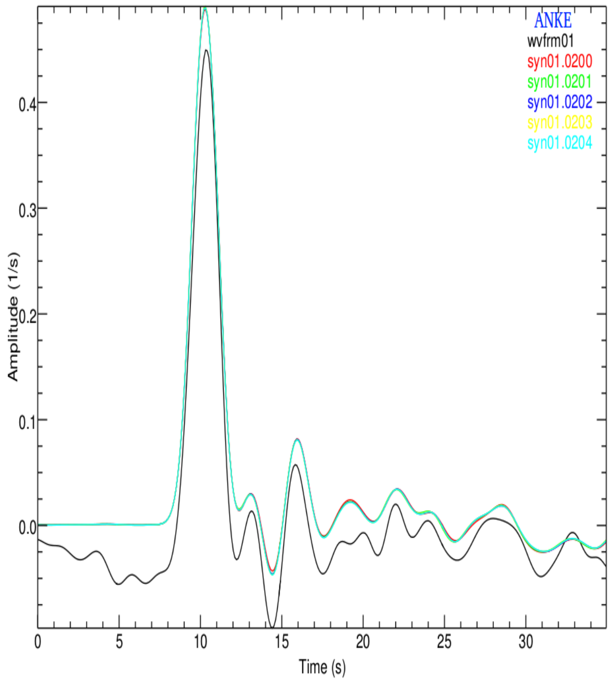

(a) ANKE

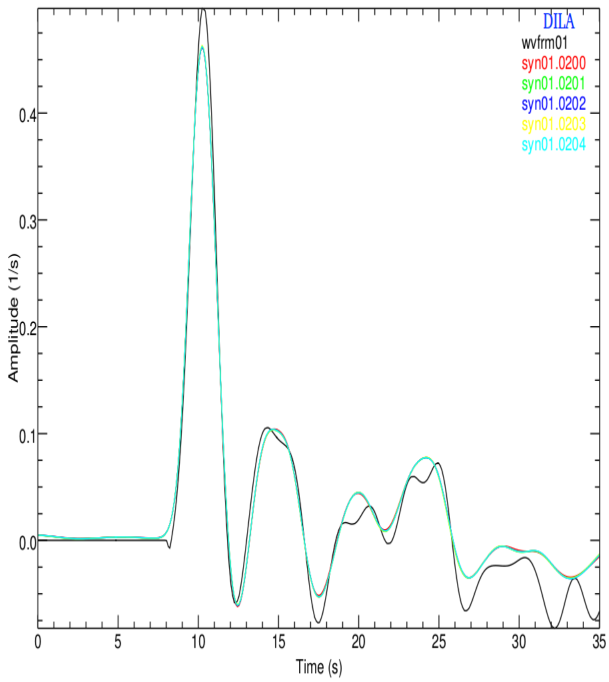

(b) DILA

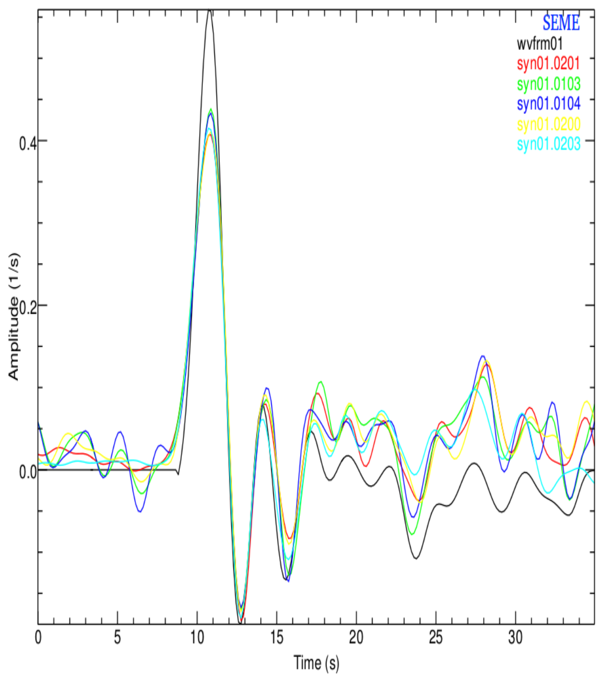

(c) SEME

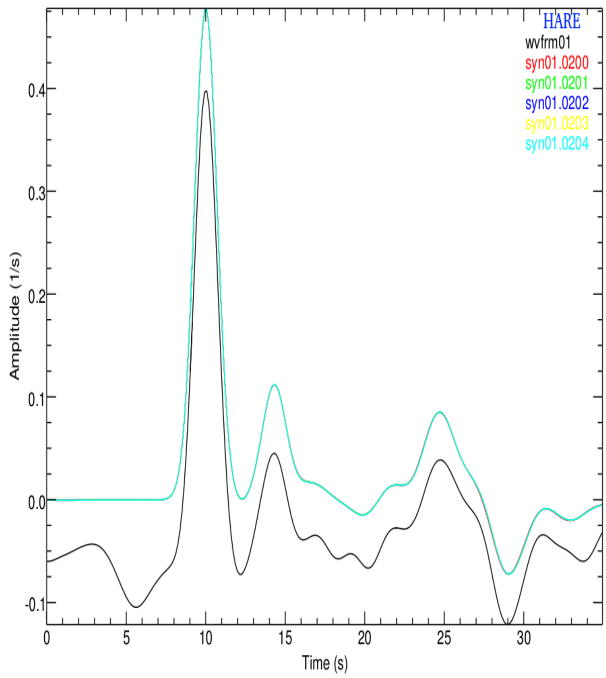

(d) HARE

Figure 5.7: Smoothest models which have been obtained by varying the smoothing weight parameter using the program "smthinv". The wvfirm01 is the observed data and the rest are the synthetic waveform.

5.7 Synthetic and Observed Waveform

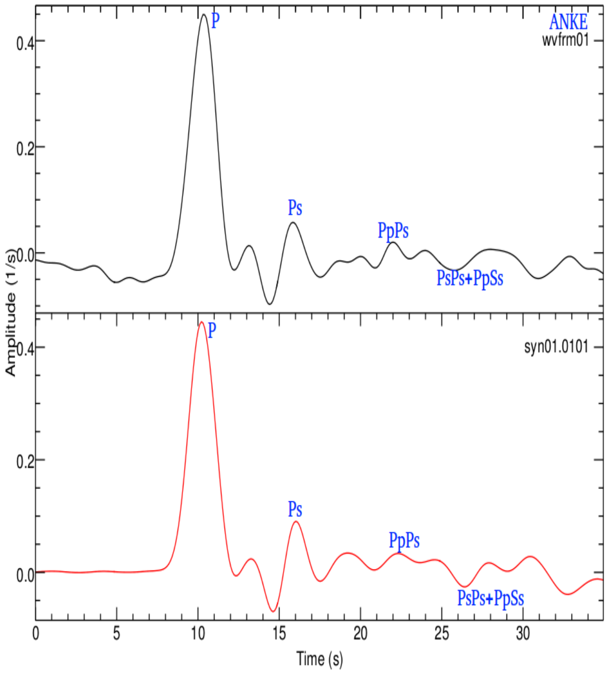

(a) ANKE

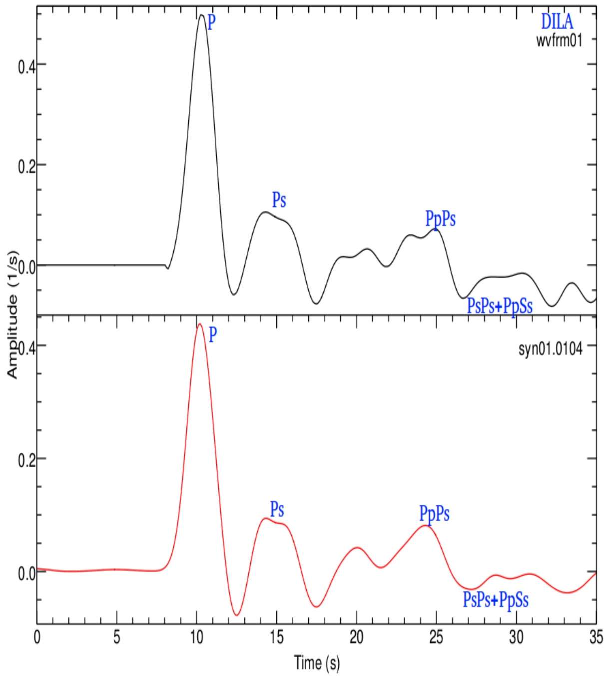

(b) DILA

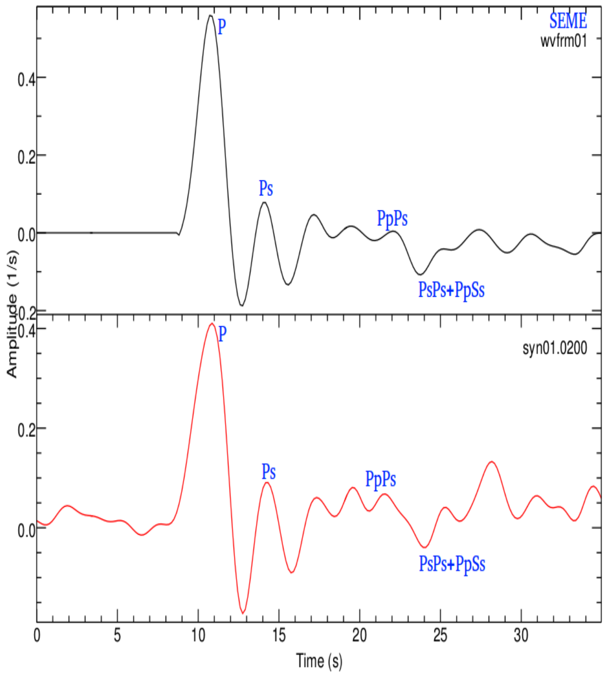

(c) SEME

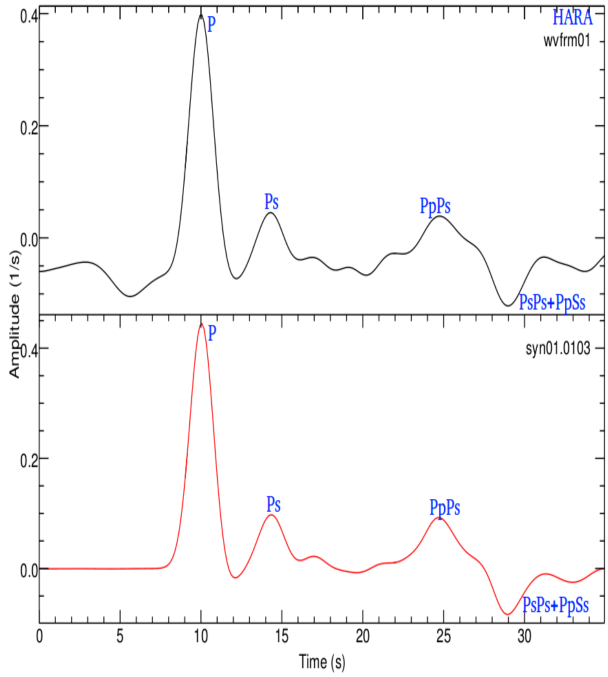

(d) HARE

Figure 5.8: The direct P-wave, Ps-Moho and the reverberations (PpPs, PpSs+PsPs) of both observed and synthetic wave form independently.

5.8 Comparative Overview Of Observed and Synthetic Waveform

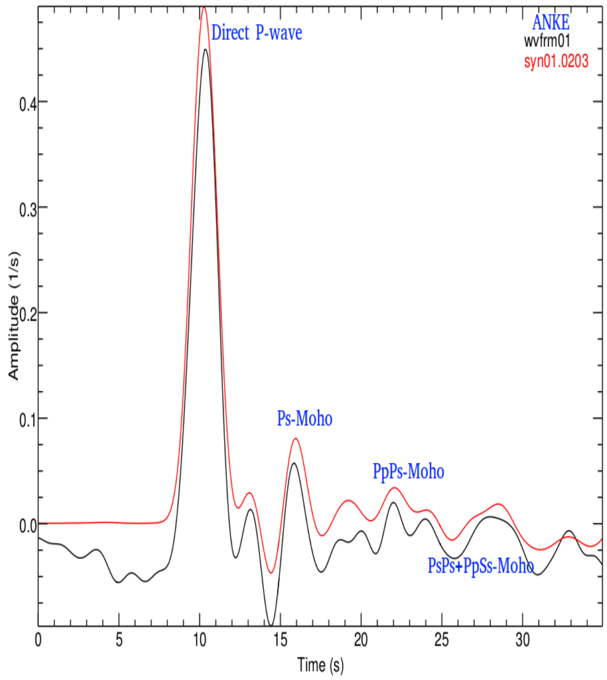

(a) ANKE

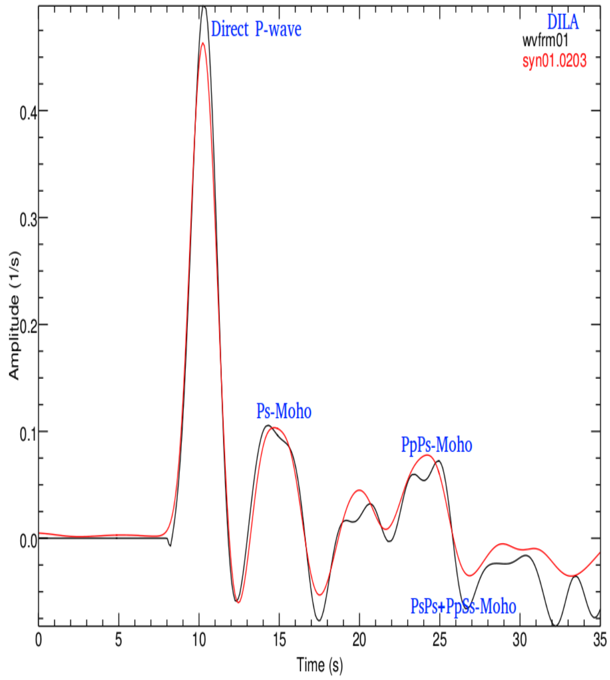

(b) DILA

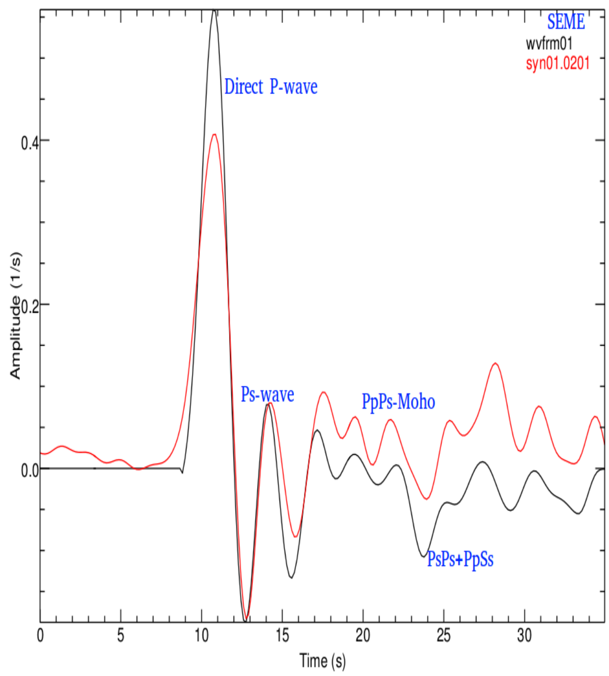

(c) SEME

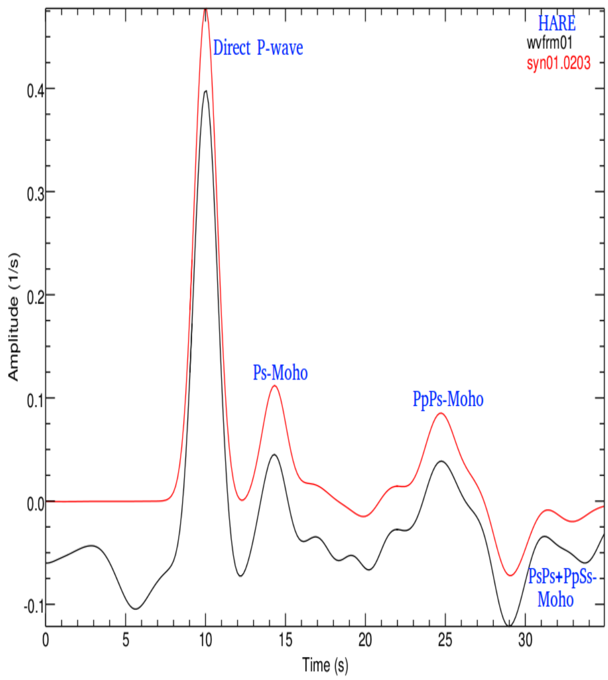

(d) HARE

Figure 5.9: A plot of observed-waveform and best of the best synthetic-waveform obtained after repeated inversion using a program "manyinv" with a composite of a cubic perturbation and a random perturbation added onto the layer velocities.

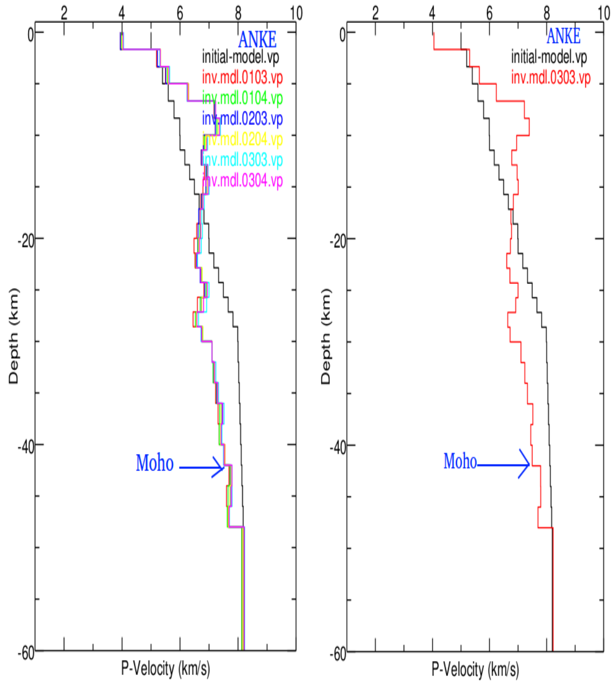

(a) ANKE

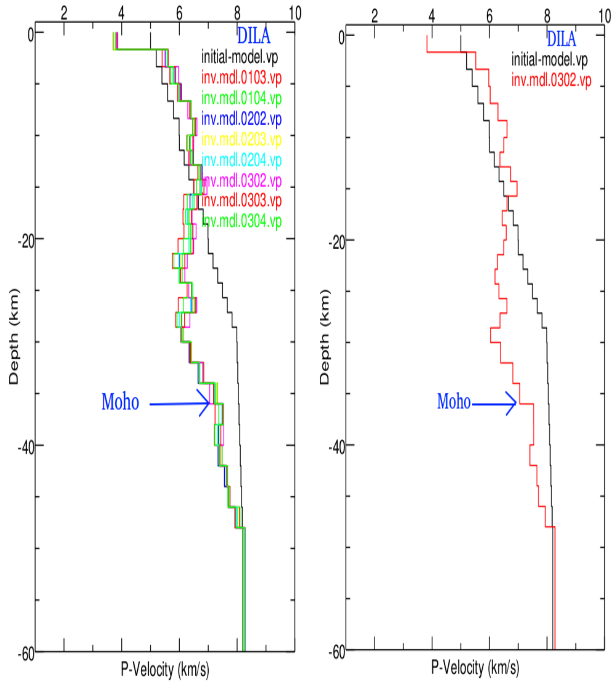

(b) DILA

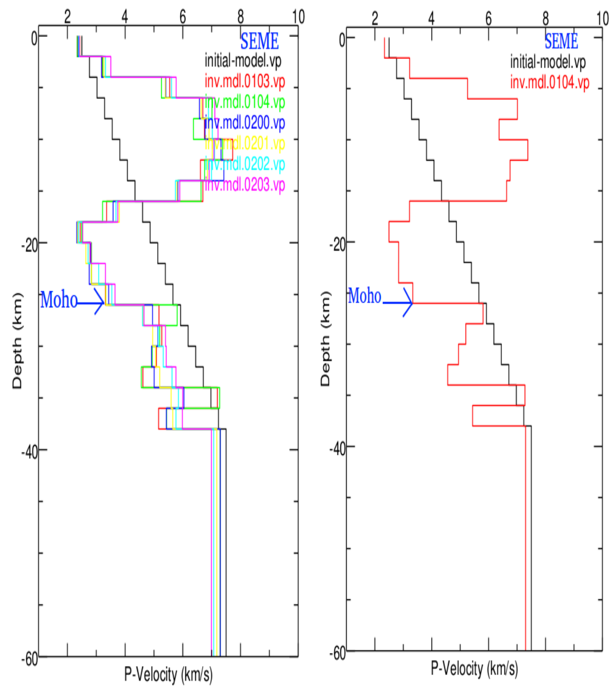

(c) SEME

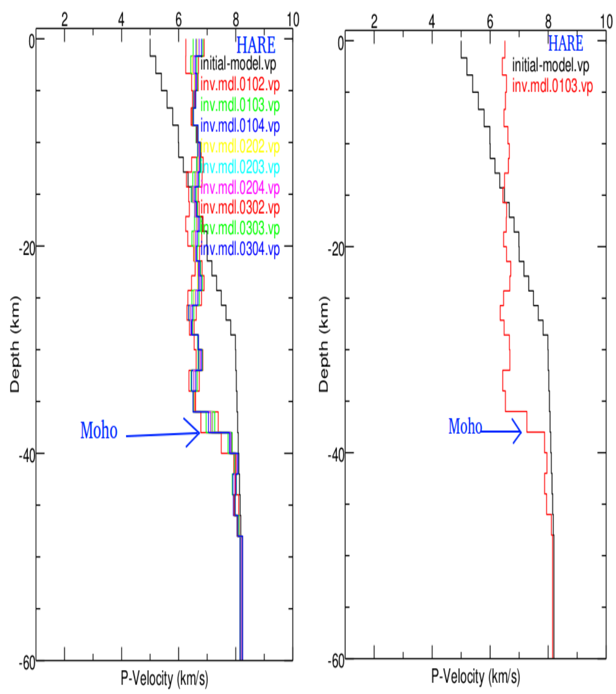

(d) HARE

Figure 5.10: The overall inversion result of receiver function and the velocity gradient obtained by adding smoothing and perturbing real values.

CHAPTER 6

DISCUSSION

From the inversion result we have obtained that in Semera (Central Afar), crustal layers up to $4km$ has a P-wave velocity $2.4-3.2\frac{km}{s}$ which seems to be a cover rock layer (e.g., sediments, volcanics). At Tendaho Graben $14km$ away from Semera lithological logs of boreholes have found sedimentary cover especially alluvial and lacustrine deposits at top most layers (Aquater., 1996; Gianelli et al., 1998 and Lewi et al., 2015). In this work, the top most layers beneath Semera seem to be volcanic covered by thin sediments. This conclusion has a similar inference with the work of Lewi (2015) (i.e thickness of sediments is not more than 1.2 km and decreases northwards to about 0.75 km) which is obtained by analysing previous lithological logs from boreholes. But, below the top layers of Semera station there is a relatively thick layer having a P-wave velocity ranging from $6.6\frac{km}{s} - 7.6\frac{km}{s}$. This high velocity layer obtained in this station is for about $8km$ thick, and this result seems in good agreement with the tomographic studies of the uppermost $15km$ of crustal structure beneath the central rift zone are underlained by high-velocity elongate bodies (Keranen et al. 2004). In similar prospect this high velocity thick layer underneath the Semera station ($6km - 14km$ from the surface) might be underplate cooled mafic magma, which are dyke intrusions and magmatic segments (e.g Keranen, 2004; Bastow, 2005). This high velocity material probably be underplate. But, beneath $16km$ from top there is unanticipated decrement of velocity for $10km$ thickness (see Table 6.1). Eventhough the value of Vp is decreasing, the aftermath of $\frac{Vp}{Vs}$ is large ($\frac{Vp}{Vs} \geq 1.8$). This means the Vs value is very small which might be due to the fact that the lower crust contains a kind of melt intrusion in which shear wave velocity decreases more than P-wave (Watanable, 1993). The low velocity zone obtained beneath Semera seem to be found beneath Tendaho Graben (south west of semera) at a distance of $\sim 14km$ away from SEME. By using gravity modeling and MT profile low density and high electrical conductivity materials have been found for a distance of $\sim 13km$ away from the Tendaho Graben for 15-28km depth in the rift axis (Johnson., 2012).

Table 6.1: The values of P-wave velocities at various depth beneath SEMERA station.

Location	P-wave velocity($\frac{km}{s}$)	Thickness of the layer from the top(km)	Remarks
SEMERA (Central Afar)	$2.4 - 3.2$	1 - 4	
	~ 5.5	4 - 6	
	$\sim$ 6.6 - 7.6	6 - 14	
	~ 5.5	14 - 16	
	$\sim 2.5 - 3.5$	16 - 26	
	~ 5	26 ± 2	Depth to Moho

The low P-wave velocity crustal materials obtained beneath Semera station in this work seem to have similar reasonings with the work of Knox et al., 1998 who used Rayleigh wave dispersion from earthquakes crossing Afar and determined uppermost uppermantle S-wave velocities. The result of S-wave velocity was about $0.2 - 0.8\frac{km}{s}$, which is slower than Preliminary Reference Earth Model (PREM) and it was infered to be partial melt. Determining the cause of seismic velocity heterogeneity within the Earth is not straightforward (Bastow, 2005). In similar manner Goes et al. 2000, suggested that a number of factors can affect seismic velocities. In the upper mantle, temperature is believed to have more influence than compositional variations (e.g. Goes et al. 2000). Other factors affecting seismic velocities are the presence of partial melt or water (Bastow, 2005). According to this study, the low velocity zones observed beneath Semera (Afar depression) might be the indication of anomalously hot upper mantle and local areas of melting or melt ponding. The suggested melt supply beneath semera could very likely be a cause of transition from continental to oceanic rifting for a similar reasonings as Bastow et al. 2005. The Moho depth beneath semera is about $\sim 26km \pm 2km$, this result likely deliver us the possible inference given by Berkhemer et al. (1975), who reported Moho depths along two refraction lines is about 30 km in the south and 26 km in the north of Afar. The imaged low-velocity anomalies beneath Semera are likely the result of temperature which creates the partial melt (Bilham et al. 1999).

Different kinematic models for rifting often ignore the effects of melt in the rifting process(e.g. Wernicke, 1985; Huismans and Beaumont, 2003). The rifting process may not only be due to the kinematic models but also due to the addition of dyke and melt (Buck, 2004). The average tectonic force required to initiate and maintain breakup may have greater magnitude than the previous result calculated with out melt impact on the rifting processes (e.g. Kusznir and Park 1987; Hopper and Buck 1993; Buck 2004). The high temperature beneath Semera may cause rifting and this seems to have a role in melt transport beneath the upper crust. The breakup between boundaries of the rift and plateau are the combined effect of lithospheric heating by magma (thinning effect) and strain accommodation by melt intrusion which facilitates crustal extension (Buck, 2004; Bastow et al. 2005). Similarly, along south central part of Red Sea Rift, using gravity modeling $13km$ broad-ranging partial melt is observed at the depth of $8.5 - 25km$. The magma reservoir at the depth of $16 - 26km$ observed beneath Semera in this work, has been observed at margin of Red Sea Rift and Tendaho Graben at the depth of $15-25km$ (Johnson., 2012 and Lewi., 2015). All the steps described in the methodology have been applied to get the above results. The results have been compared with the previous works done in the region and found to be very good to apply for the other stations.

In the case of Ankober (western plateau), a p-wave velocity ranging from $4.0\frac{km}{s} - 7.8\frac{km}{s}$ has been obtained beneath the station for a varying thicknesses (see Table 6.2). The Moho depth is located at the depth of $42km \pm 1.7km$. The high velocity zone located beneath $7km - 10km$ seems to be cooled magma. The location of this high velocity zone in the upper crust beneath Ankober station might be caused by cooled mafic magmatic intrusion as reported by Keranen et al. 2004 for central rift having ($Vp = 6.5\frac{km}{s}$). The depth to Moho beneath Ankober, western plateau, obtained in this study has good agreement with the previous studies (e.g Mahatsente et al., 1999, Mammo, 2013, Dugda et al., 2005 and Stuart et al., 2006) which are comparable and concomitant Western plateau Moho depth result (see Table 2.1 and Table 2.2)

Table 6.2: The values of P-wave velocities at various depth beneath ANKOBER station.

Location	P-wave velocity($\frac{km}{s}$)	Thickness of the layer from the top(km)	Remarks
ANKOBER (NW plateau)	$4.2 - 6.2$	1 - 7	
	~ 7.1	7 - 10	
	$6.7 - 7.0$	10 - 30	
	$7.1 - 7.5$	30 - 42	
	~ 7.8	42 ± 1.7	Depth to Moho

In addition to the Moho depth, the result of P-wave velocity has many implication regarding subsurface lithology. In Ankober the high velocity intrusion is predominantly found at various depths of the upper and lower crust having P-wave velocities which are about $\geq 7\frac{km}{s}$ as seen in table 6.2. These values might be cooled magma which seem to be in good agrement with the results obtained in the previous studies (Dugda, 2005 and Hammond, 2011). In this work beneath $30km$ depth the velocity is ranging from $7.1 - 7.5\frac{km}{s}$ for a significant thickness and this probably be subcrustal cooled body. A similar argument was given by Cornwell et al. 2006 at a depth of $33km$ beneath north west plateau subcrustal underplate igneous body has been inferred to have a velocity of $Vp = 7.38\frac{km}{s}$ for $15km$ thickness. A significant velocity contrast was observed at a depth of $42km \pm 2km$ with a P-wave velocity of about $\sim 7.8\frac{km}{s}$. This result could be due to the existence of Moho interface. The teleseismic RFs inversion result of Ankober seem to show that most of the upper and lower crustal P-wave velocity is in the range of $6.7 - 7.2\frac{km}{s}$ and the petrologic implications of this value might be the domination of mafic lithologies. Compressional velocity is a determinant factor that can manifest the mineral composition of crust and uppermost mantle (Juli, 2005). A similar reasonings has been given by Dugda et al. 2006 the average velocity Vp increased towards the western plateau and the reason for this increment be hapened due to the existence of a mafic composition magmatic underplate caused by dyking.

Table 6.3: The values of P-wave velocities at various depth beneath DILA station.

Location	P-wave velocity($\frac{km}{s}$)	Thickness of the layer from the top(km)	Remarks
DILA	$4.0 - 6.0$	1 - 8	
	$6.0 - 7.0$	8 - 36	
	~ 7.53	36 ± 2	Depth to Moho

Likewise, a similar attribute was remarked in Dila (south-eastern plateau) near the rift margin. Beneath this station the value of Vp at different depths were found to be less hetrogeneous (i.e ranging from $6.0 - 7.0\frac{km}{s}$) as seen in table 6.3. There is a relatively high velocity contrast at the depth of $36km$ from the top. This incongruity of velocity at this interface might be due to the Moho interface. The Moho layer is located at the depth of $36km \pm 2km$ from the surface. There is a relatively high velocity zone located beneath $8km$ and above $29km$. The velocity of the layer below $36km$ from the surface has a relative drastic change which is about $7.53\frac{km}{s}$. This velocity contrast at the depth of $36km$ might be due to the existence of the Moho depth beneath Dila station, which is located at the south eastern plateau and it is very close to the southern main Ethiopian rift margin.

The Moho depth beneath the eastern and southeastern plateau have been studied by many researchers. These research work have been done by different geophysical methods especially 2-D and 3-D gravity modeling and teleseismic receiver functions (Makris, 1972; Mahatsente, 1999; Dugda, 2005 and Hammond 2011). In this work the moho depth beneath Dila is about $36 \pm km$ with a velocity value of $7.53\frac{km}{s}$. This result seems to be very close to the findings of 3-D gravity modeling of Mahatsente et al., 1999, which is in the range of $34-38km$. The moho depth underneath Dila station also has a very close resemblance with the result obtained by Mamo (2013), in which the southern end of the rift has a Moho depth of about $\sim 38km$. And, the Moho depth obtained in this work might be due to the fact that Dila is located in the southern rift margin, and this result seems to be in close resemblance with the work of Mamo (2013). According to Mamo (2013) the result of gravity modeling and teleseismic receiver function might have a significant deviation of about $\pm 2km$.

Table 6.4: The values of P-wave velocities at various depth beneath HARAR stations.

Location	P-wave velocity($\frac{km}{s}$)	Thickness of the layer from the top(km)	Remarks
HARAR	$\sim 6.3-6.8$	Most Upper and Lower Crust	
	$7.2-7.8$	36 - 38	
	~ 8.0	38 ± 2	Depth to Moho

The final and comparable scoreline was noticed in Harar (north-eastern plateau) near the rift margin. Beneath this station the value of Vp at different depths are listed in the above table (Table 6.4).

The Moho interface is located at the depth of $38km \pm 2km$ from the surface. There is a surprisingly drastic change of P wave velocity from $7.8\frac{km}{s}$ to $8.0\frac{km}{s}$. The velocity contrast at the depth of $38km$ could be the location of Moho interface of Harar. The Moho depth obtained in this study seems to be close with the result of Mamo (2013) at the southern Afar (Junction with MER), which is about

$\sim 28km$ as seen in table 6.4. Harar is very close to the southern Afar margin and this could be the fact for the Moho depth beneath Southern Afar and north eastern plateau are close. There could be a certain relation between the larger Moho depth underneath southern Afar (compared to northern and eastern Afar) and relatively smaller Moho depth beneath north eastern plateau margin (compared to western plateau). The Moho depth underneath Afar depression is very small compared to the other Rift segments and the remaining plateaus (Makris, 1972; Mamo, 2004; Dugda, 2005; Hammond, 2011; Mamo, 2013 and Makris, 1991). However, the depth is not equal in all areas of Afar, the depth of Moho interface increases down to the southern Afar (e.g Makris, 1991; Mamo, 2004; Dugda, 2005; Hammond, 2011 and Mamo, 2013). But, according to this study the Moho depth seems to increases towards Harer. According to Makris et al. 1991 and Makris et al. 1997, the Moho depth beneath southern Afar, and eastern edge plateau was investigated using 2-D gravity modeling (bouguer anomaly). The result was found to be $22 - 25km$ (southern Afar) and $\sim 30km$ (eastern edge plateau). Mahatsente et al., 1999 conveyed the Moho depth of north eastern plateau is ranging from $34km$ to $42km$. The upshot of inversion from teleseismic broad band events using receiver function method was done for Harer which is about $38 \pm 2km$. The end result of moho depth of Harar from our inversion seems to be in conformity with the work of previous results (e.g Makris, 1991; Mahatsente et al., 1999; Mamo, 2004; Dugda, 2005; Hammond, 2011 and Mamo, 2013). The depth variations among southern Afar and north eastern plateau (e.g Harar) are very likely to be due to the formation of underplate above the Moho interface. Likewise, the Moho depth variations among Northern Afar and central Afar (e.g Semera) and north western plateau (e.g Ankober) are probably due to the formation of underplate above the Moho interface. In both cases the addition of root zone, in Airy style compensation and the intruded magmatic plume that might have been established regional upper mantle velocity and density contrast (e.g Mamo, 2013 and referenced therein).

CHAPTER 7

CONCLUSIONS AND RECOMMENDATION

By applying all the steps described in the methodology appreciable results have been obtained. The results have been compared with the conclusions inferred in previous works around the region and found to be very good. First, all the required steps in RFs technique were implemented in Semera and appreciable results were found. Beneath Semera station for about $\sim 4km$ depth the value of Vp is in the range of $2.4 - 3.2\frac{km}{s}$ and this might notify that the surface is composed of sediments and volcanics. A thickness of about $8km$ beneath the station has a velocity in the range of $\sim 6.6\frac{km}{s} - \sim 7.6\frac{km}{s}$, which is very high compared to the remaining thicknesses. This probably be an indispensable manifestation of cooled magmatic body. In contrast, underneath $16km$ depth from the top the value of Vp is between $\sim 2.5\frac{km}{s}$ and $\sim 3.5\frac{km}{s}$ for about 10km thickness, this might also be due to melt intrusion or partial melt intrusion. This melt region might be cause of transition from continental to oceanic rifting. In this work the Moho depth beneath Semera is about $26km \pm 2km$. Whereas in Ankober there is an astonishing velocity contrast between $\sim 7km$ and $\sim 20km$ down from the surface. This immense velocity contrast at this depth might be due to the existence of cooled magmatic intrusion. At the depth of $35km$, $Vp \sim 7.5\frac{km}{s}$, this might be due to cooled magma from previous dike or sill intrusions beneath ANKE station. Below this layer, there has been a momentous velocity contrast. Therefore, the Moho depth beneath Ankober is estimated at $42 \pm 1.7km$ ($\sim 7.8\frac{km}{s}$). In view of the fact that most of the velocities of the upper and lower crust of Ankober is in the range of $6.2\frac{km}{s}$ to $7.5\frac{km}{s}$ and this might be due to the essence of cooled mafic rock underlined beneath the surface. Moreovere, the inversion result obtained for Dila station revealed that most of the P-wave velocities among different layers are in the range of of $6\frac{km}{s} - 6.6\frac{km}{s}$. The value of Vp below 36km depth from the surface of Dila is about $7.53\frac{km}{s}$ and this velocity at this interface is relatively larger than the upper layer. This high P wave velocity value recorded at the depth of $36 \pm 2km$ beneath Dila might be an estimate of Moho interface. Ultimately, the teleseismic events recorded in Harar has been analysed and Vp seem to be large in most parts of the crust. The Vp result obtained beneath Harar station might notify that the upper and lower crust has less heterogeneity. This work estimated the Moho depth beneath Harar station to be about $38 \pm 2km$. Finally, we recommend that to apply instantaneous velocities rather than average velocity to get a refined P-wave velocities beneath each stations to identify thin layers in receiver function techniques. In addition to this, we highly recommend that a stochastic Montecarlo approach could be applied for receiver function analysis.

BIBLIOGRAPHY

[1] Ammon, C.J., Randall, G.E. and Zandt, G. (1990). *On The Nonuniqueness of Receiver Function Inversion*. J. geopys., **95**: 15303-15318.

[2] Ammon, C. J. (1991). *The isolation of receiver effects from teleseismic P waveforms*. Bull. Seism. Soc., **81**: 2504-2510.

[3] Amukti, R., Suryanto, W. and Suharno. (2015). *Subsurface Structure Model of Mount Merapi Using Receiver Function*. Proceedings World Geothermal Congress 2015. Melbourne, Australia, 19-25

[4] Annen, C. and Sparks, R. S. J. (2002). *Effects of repetitive emplacement of basaltic intrusions on thermal evolution and melt generation in the crust*. Earth Planet. Sci. **203**, 937-955.

[5] Aquater (1996). *Tendaho Geothermal Project Final Report, II*. Ministry of Mines and Energy, Ethiopian Institute of Geological Survey, Addis Ababa.

[6] Ayalew, D., Barbey, P., Marty, B., Reisberg, L., Yirgu, G. and Pik, R. (2002). *Source, genesis and timing of giant ignimbrite deposits associated with Ethiopian continental flood basalts*. Geochim. Cosmochim. Acta., **66**: 1429-1448.

[7] Ayalew, D. and Yirgu, G. (2003). *Crustal contribution to the genesis of Ethiopian plateau rhyolitic ignimbrites: Basalt and rhyolite geochemical provinciality*, J. Geol. Soc. London, **160**: 47-56.

[8] Ayele, A., Stuart, G. and Kendall, J. M. (2004). *Insights into rifting from shear wave splitting and receiver functions: An example from Ethiopia*. Geophys. J. Int., **157(1)**: 354-362.

[9] Ayele, A., Jacques, E., Kassim, M., Kindane, T., Omar, A., Tait, S., Nercessian, A., Dechabalier, J.B. and King, G. (2007). *The volcano-seismic crisis in Afar, Ethiopia, starting September 2005, Earth Planet*. Sci. Lett. **255**: 177187.

[10] Bastow, I. D., Graham, W. S., Michael J. K. and Ebinger, C. J. (2005). *Upper-mantle seismic structure in a region of incipient continental breakup: northern Ethiopian rift*. J. Geophys. Int., **162**: 479-493

[11] Bastow, I. D., Nyblade. A. A., Stuart. G. W., Rooney. T. O., and Benoit. M. H. (2008). *Upper mantle seismic structure beneath the Ethiopian hot spot: Rifting at the edge of the African low-velocity anomaly*. Geochem. Geophys. Geosyst., **9**, Q12022, doi:10.1029/2008GC002107.

[12] Behle, A., Makris, J., Baier, J. and Delibasis, N., (1975). *Salt thickness near Dallol (Ethiopia) from seismic reflection measurements and gravity data, in Afar Depression of Ethiopia: Proceedings of an International Symposium on the AfarRegion and Related Rift Problems*. Held in Bad Bergzabern, FR Germany, April 1-6, 156-167, Schweizerbart, Stuttgart, Germany.

[13] Berckhemer, H. (1975). *Afar Depression of Ethiopia, in Schweizerbart*, scheVerlagsbuchhandlung Science Publishers, Stuttgart. **1**: 89-107

[14] Berktold, A., Haak, V. and Angeheister, G. (1975). *Magnetotelluric measurements in the Afar area*. In: A. Pilger and A. Rosler (Editors), Afar Depression of Ethiopia. Schweizerbart, Stuttgart, Vol. I, pp. 66-79.

[15] Bilham, R., Bendick, R., Larson, K., Mohr, P., Braun, J., Tesfaye, S. and Asfaw, L. (1999). *Secular and tidal strain across the Main Ethiopian Rift*. Geophys. Res. Lett., **26**: 2789-2792.

[16] Boccaletti, M., Bonini, M., mazzuoli, R., Abebe, B., Piccardi, L. and Tortorici, L. (1998). *Quaternary oblique extensional tectonics in the Ethiopian Rift (Horn of Africa)*. Tect. phys., **287**: 97-116.

[17] Buck, W. R., Karner, G.D., Taylor, B., Driscoll, N. W. and Kohlstedy, D. L. (2004). *Consequences of asthenospheric variability on continental rifting. In Rheology and Deformation of the Lithosphere at Continental Margins*, Columbia University Press, New York, 1-30.

[18] Bullen, K.E. and Bolt, B.A. (1947). *An Introduction to the Theory of Seismology*. Cambridge University Press, Cambridge.

[19] Burdick, L.J. and Langston, C.A. (1977). *Modeling crustal structure through the use of converted phases in teleseismic body-wave forms*, Bull. seism. Soc. Am., **67**: 677-691.

[20] Cassidy, J.F. (1992). *Numerical experiments in broadband receiver function analysis*. Bull. Seismol. Soc., **82**: 1453-1474.

[21] Chevrot, S. and Hilst, R. D. (2000). *The Poisson ratio of the Australian crust: geological and geophysical implications*. Eart. Planet. Sci. Lett., **183**: 121- 132.

[22] Chorowicz, J., Collet, B., Bonavia, F.F. and Korme, T. (1994). *Northwest to north-northwest extension direction in the Ethiopian Rift deduced from the orientation of extension structures and fault-slip analysis*. Bull. Geol. Soc. Am., **105**: 1560-1570.

[23] Christensen, N. I. and Mooney, W. D. (1995). *Seismic velocity structure and composition of the continental crust: a global view*. J. Geophys. Res., **100**: 9761-9788.

[24] Clayton, R.W. and Wiggins, R.A. (1976). *Source shape estimation and deconvolution of teleseismic body waves*. Geophys. J. R. Astron. Soc., **47**: 151-177.

[25] Clitheroe, G., Gudmundsson, O. and Kennett, B. L. N. (2000). *Sedimentary and upper crustal structure of Australia from receiver functions*. Australian Journal of Earth Sciences., **47**: 209-216.

[26] Cornwell, D. G., Mackenzie, G. D., England, R. W., Maguire, P. K. Asfaw, H. L. M. and Oluma, B. (2006). *Northern Main Ethiopian Rift crustal structure from new highprecision gravity data, in The Afar Volcanic Province Within the East African Rift System, edited by G. Yirgu, C. J. Ebinger, and P. K. H. Maguire*. Geol. Soc. Spec. Publ., **259**: 307-321.

[27] Cornwell, D. G., Magurie, P. K. H., England, R. W. and Stuart, G. W. (2010). *Imaging detailed crustal structure and magmatic intrusion across the Ethiopian rift using a dense linear broadband array*. Geochem. Geophys. Geosyst., **11**: Q0AB03, doi:10.1029/2009GC002637.

[28] Christensen, N. I. (1996). *Poissons ratio and crustal seismology*. J. Geophys. Res., **101(B2)**: 3139-3156.

[29] Daly. E., Keir. D., Ebinger. C. J., Stuart. G. W., Bastow. I. D., Ayele. A. (2008). *Crustal tomographic imaging of a transitional continental rift: the Ethiopian rift* Geophys. J. Int., **172**, 1033-1048

[30] Davidson, A., and Rex, D. C. (1980), *Age of volcanism and rifting in souhern Ethiopia*, Nature, **283**, 657-658.

[31] Desissa, M., Johnson, N. E., Whaler, K. A., Hautot, S., Fisseha, S. and Dawes, G. J. K. (2013). *A mantle magma reservoir beneath an incipient mid-ocean ridge in Afar, Ethiopia*. Nature Geoscience, **6**, 861-865, http://doi.org/10.1038/ngeo1925

[32] Didana, Y. L., Thiel, S. and Heinson, G. (2014). *Magnetotelluric imaging of upper crustal partial melt at Tendaho graben in Afar, Ethiopia*. Geophysical Research Letters, **41**, 3089 3095, http://doi.org/10. 1002/2014GL060000

[33] Dugda, M. T., Nyblade, A. A., Julia, J., Langston, C. A. Ammon, C. J. and Simiyu, S. (2005). *Crustal structure in Ethiopia and Kenya from receiver function analysis: Implications for rift development in eastern Africa*. J. Geophys. Res., **110**: B01303, doi:10.1029/2004JB003065.

[34] Dugda., M. T. and Nyblade, A. A. (2006). *New constraints on crustal structure in eastern Afar from the analysis of receiver functions and surface wave dispersion in Djibouti*. Geo. Soc. London., **259**: 239-251.

[35] Ebinger, C. J., Yemane, T. G., WoldeGabriel, J. L. and Walter, R. C. (1993). *Late Eocene-Recent volcanism and faulting in the southern main ethiopian rift*, J. Geol. Soc., **150(1)**, 99-108.

[36] Ebinger, C. J. and Casey, M. (2001). *Continental breakup in magmatic provinces: An Ethiopian example*. Geology., **29(6)**: 527-530.

[37] Ebinger, C. J., Yemane. T., Woldegabriel. G., Aronson. J. L., and Walter. R. C. (1993), *Late Eocene-Recent volcanism and faulting in the southern Main Ethiopian Rift*. J. Geol. Soc., **150**, 99-108.

[38] Fuchs, K., Altherr, R., Muller, B. and Prodehl. (1997). *Structure and Dynamic Processes in the Lithosphere of the Afro-Arabian Rift System*. Tectonophysics., **278(1-4)**: 329-352.

[39] Furman, T., Bryce. J., Rooney. T., Hanan. B., Yirgu. G., and Ayalew. D. (2006). *Heads and tails: 30 million years of the Afar plume, in The Afar Volcanic Province within the East African Rift System*. edited by Yirgu. G., Ebinger. C. J., and Maguire. P. K. H., Geol. Soc. Spec. Publ., **259**, 95-119.

[40] Gallardo, L.A , Meju, M A. (2004). *Joint two-dimensional cross-gradient imaging of magnetotelluric and seismic traveltime data for structural and lithological classification*. J. Geophys., **169(3)**: 1261-1272.

[41] Gani, N. D. S., Gani, M. R., and Abdelsalam, M. G. (2007). *Blue Nile incision on the Ethiopian Plateau: Pulsed plateau growth, Pliocene uplift, and hominin evolution*. GSA Today, **17(9)**: 4-11, doi:10.1130/GSAT01709A.1.

[42] Gianelli, G., Mekuria, N. (1998). *Water-rock interaction and hydrothermal mineral equilibria in the Tendaho geothermal system*. Jou. Volcanology and Geothermal Res., **86**, 253 - 276.

[43] Goes, S.,Spakman, W. and Bijwaard, H. (1999). *A lower mantle source for Central European volcanism*. Science, **286**: 1928-1931.

[44] Goldstein, P. (1999). *SAC's user's manual*. Lawrence-Livermore Laboratory, University of california.

[45] Hammond, J. O. S., Kendall, J. M., Stuart, G. W., Keir, D., Ebinger, C. and Belachew, M. (2011). *The nature of the crust beneath the Afar triple junction: Evidence from receiver functions*. Geochem. Geophys. Geosyst., **12**: Q12004, doi:10.1029/2011GC003738.

[46] Hayward, N. J. and Ebinger, C. J. (1996). *Variations in along axis segmentation of the Afar rift system*. Tectonics. **15(2)**: 244257, doi:10.1029/95TC02292.

[47] Hofmann, C., Courtillot, V., Feraud, G., Rochette, P., Yirgu, G. Ketefo, E. and Pik, R. (1997). *Timing of the Ethiopian flood basalt event and implications for plume birth and global change*. Nature, **389(6653)**: 838-841.

[48] Hopper, J. and Buck, W. (1993). *The initiation of rifting at constant tectonic force: the role of diffusion creep*. J. geophys. Res., **98**: 213-221.

[49] Huismans, R. and Beaumont, C. (2003). *Symmetric and asymmetric lithospheric extension: relative effects of frictional plastic and viscous strain softening*. J. geophys. Res., **108(B10)**: 2496, doi:10.1029/2002JB002026.

[50] Jesse F. L. and Douglas A. W. (2004). *Combined Receiver-Function and Surface Wave Phase-Velocity Inversion Using a Niching Genetic Algorithm: Application to Patagonia*. Bull. Seis. Soc. Am., **94**: 977-987

[51] Johnson, N. (2012). *Magnetotelluric studies of the crust and upper mantle in a zone of active continental breakup, Afar, Ethiopia*. PhD thesis, University of Edinburgh.

[52] Juli, J., Ammon, C. J. and Nyblade, A. A. (2005). *Evidence for mafic lower crust in Tanzania, East Africa, from joint inversion of receiver functions and Rayleigh wave dispersion velocities*. Geophys. J. Int., **162**: 555-569

[53] Keir, D., Stuart, G. W., Jackson, A. and Ayele, A. (2006). *Local earthquake magnitude scale and seismicity rate for the Ethiopian rift*. Bull. Seismol. Soc. Am., **96**: 2221-2230, doi:10.1785/0120060051.

[54] Keir, D., Hamling, I., Ayele, A., Calais, E., Ebinger, C., Wright, T.J., Jacques, E., Mohammed, K., Hammond, J.O.S., Belachew, M., Baker, E., Rowland, J.V., Lewi, E. and Bennati, L. (2009). *Evidence for focused magmatic accretion at segment centers from lateral dike Injections captured beneath the Red Sea rift in Afar*. Geology, **37**: 59-62.

[55] Kendall, J. M., Stuart, G. W., Ebinger, C.J., Bastow, I. D. and Keir, D. (2005). *Magma assisted rifting in Ethiopia*, Nature., **433**: 146148.

[56] Keranen, K., Klemperer, S. L., Gloaguen, R., and Group, E. W. (2004). *Three-dimensional seismic imaging of a protoridge axis in the Main Ethiopian rift*. Geology., **32(11)**: 949-952.

[57] Knox, R., Nyblade, A. and Langston, C. (1998). *Upper mantle S velocities beneath Afar and western Saudi Arabia from Rayleigh wave dispersion*. Geophys. Res. Lett., **25**: 4233-4236.

[58] Kusznir, N. and Park, R. (1987). *The extensional strength of the continental lithosphere: its dependence on geothermal gradient, and crustal composition and thickness, in Continental Extensional Tectonics*. Geo. Soc. Spec. Pub., **28**: 35-52.

[59] Langston, C.A. (1977). *The effect of planar dipping structure on source and receiver responses for constant ray parameter*. J. Geophys., **67**: 1929-1050.

[60] Langston, C. A. (1979). *Structure under Mount Rainier, Washington, inferred from teleseismic body waves*. J. Geophys., **84**: 4749-4762.

[61] Levin, V. and Park, J. (1997). P-SH conversions in a flat-layered medium with anisotropy of arbitrary orientations, Geophys. J. Int., **131**: 253-266.

Lewi, E., Keir, D., Birhanu, Y., Blundy, J., Stuart, G., Wright, T. and Calais, E. (2015). *Use of a high-precision gravity survey to understand the formation of oceanic crust and the role of melt at the southern Red Sea rift in Afar, Ethiopia*. Geological Society of London, **420**, http://doi.org/10.1144/SP420.13

[62] Li, S. and Mooney, W.D. (1998). *Crustal structure of China from deep seismic sounding profile*. Tectonophysics., **288**: 105-113.

[63] Lodge, A. and Helffrich, G. (2009). *Grid search inversion of teleseismic receiver functions*. Geophys. J. Int., **178**: 513-523

[64] Mackenzie, G. D., Thybo, H. and Maguire, P. K. H. (2005). *Crustal velocity structure across the Main Ethiopian Rift: results from twodimensional wideangle seismic modelling*. Geophys. J. Int., **162(3)**: 994-1006.

[65] Mechie, J. and Prodehl, C. (1988) *Crustal and uppermost mantle structure beneath the Afro-Arabjan rift system*. Tech. Phys. 153 (1988) 103-121

[66] Maguire, P. K. H., Yirgu, G., Ebinger, C. J. and Maguire, P. K. H. (2006). *Crustal structure of the northern Main Ethiopian Rift from the EAGLE controlled-source survey: A snapshot of incipient lithospheric breakup, in The Afar Volcanic Province Within the East African Rift System*. Geol. Soc. Spec. Publ., **259**: 269-292.

[67] Mahatsente, R., Jentzsch, G. and Jahr, T. (1999). *Crustal structure of the Main Ethiopian Rift from gravity data: 3-dimensional modeling*. Tectonophysics, **313**: 363-382

[68] Makris, J., Menzel, H. and Zimmermann, J. (1972). *A preliminary interpretation of the gravity field of Afar, northeast Ethiopia*. Tectonophysics, **15(1/2)**: 1-9

[69] Makris, J. and Ginzburg, A. (1987). *The Afar Depression: Transition between continental rifting and seafloor spreading*. Tectonophysics, **141**: 199-214.

[70] Makris, J., Henke, C. H., Egloff, F. and Akamaluk, T. (1991) *The gravity field of the Red Sea and East Africa*. Tectonophysics, **198**: 369-381

[71] Mammo, T. (2004). *Mapping the Crust-Mantle Boundary Beneath Afar Depression*. Gondwana Research, K 7, **3**: 855-861.

[72] Mammo, T. (2013). *Crustal Structure of the Flood Basalt Province of Ethiopia from Constrained 3-D Gravity Inversion*. Pure Appl. Geophys., pp 1-22,DOI 10.1007/s00024-013-0663-0

[73] Mangino, S. G., Zandt, G. and Ammon, C. J. (1993). *The receiver structure beneath Mina, Nevada*, Bull. Seism. Soc. Am. **83**: 542-560.

[74] Midzi, V. and OttemoEller, L. (2001). *Receiver function structure beneath three southern Africa seismic broadband stations*. Tectonophysics. **339**: 443-454.

[75] Mohr, P.A. (1967). *The Ethiopian Rift system*. Bull. Geoph. Obser. Addis Ababa. **11**: 1-65.

[76] Mohr, P. (1983). *Ethiopian flood basalt province*, Nature, **303**: 577-584.

[77] Mohr, P. (1989). *Nature of the crust under Afar: new igneous, not thinned continental*. Tectonophysics, **167**: 1-11.

[78] Owens, T. J., Steven, R. T., George, Z. (1987). *Crustal structure at regional seismic test network stations determined from inversion of broadband teleseismic P waves*. Bull. Seism. Soc. Am. **77**: 631-662.

[79] Owens, T. J., Crosson, R. S., and Hendrickson, M. A. (1988). *Constraints on the subduction geometry beneath western Washington from broadband teleseismic waveform modeling*. Bull. Seismol. Soc., **78**: 1319-1334.

[80] Pik, R., Marty, B., Carignan, J. and Lave, J. (2003). *Stability of the Upper Nile drainage network (Ethiopia) deduced from (U-Th)/He thermochronometry: Implications for uplift and erosion of the Afar plume dome*. Earth Planet. Sci. Lett., **215(1-2)**: 73-88.

[81] Press, W. H., Teukolsky, S. A., Vetterling, W. T. and Flannery, B. P. (1997). *Numerical Recipes in Fortran 77 The Art of Scientific Computing*.second ed. University of Cambridge., **V2**, pp.490-520.

[82] Prodehl, C. and Mechie, J. (1991). *Crustal thinning in relation ship to the evolution of the AfroArabian rift system: A revew of seismicrefraction data*. Tectonophysics, **198**: 311-327.

[83] Prodehl, C., Keller, G. R. and Khan, M. A. (1994). *Crustal and upper mantle structure of the Kenya Rift*. Tectonophysics, **236**: 1-483.

[84] Randall, G. E. (1989). *Efficient calculation of differential seismograms for lithospheric receiver functions*. Geophys. J . Int., **99**: 469-481

[85] Rooney, T. T., Furman. T., Yirgu. G., and Ayalew . D. (2005), *Structure of the Ethiopian lithosphere: Evidence from mantle xenoliths*. Geochim. Cosmochim. Acta, **69(15)**, 3889-3910, doi:10.1016/j.gca.2005.03.043.

[86] Ruegg, J. C. (1975). *Main results about the crustal and upper mantle structure of the Djibouti region (T. F. A. I.), In Afar Depression of Ethiopia*, edited by A. Pilger and A. Rosler, E. Schweizerbart, Stuttgart, W. Germany, 120-134

[87] Sheriff, R.E. and Geldart, L.P. (1982). *Exploration Seismology*. Cambridge University Press, New York, **1**: 82-101.

[88] Stankiewicz, J., Sebastien, C., Rob D. V. and Maarten, J. D. (2002). *Crustal thickness, discontinuity depth, and upper mantle structure beneath southern Africa: constraints from body wave conversions*. Phys. Earth and Planetary Interiors., **130**: 235-251

[89] Stuart, G., Bastow, I. D. and Ebinger, C. J. (2006), *Crustal structure of the northern Main Ethiopian Rift from receiver function studies, in The Afar Volcanic Province Within the East African Rift System, edited by G. Yirgu, C. J. Ebinger, and P. K. H. Maguire*, Geol. Soc. Spec. Publ., **259**: 253-267.

[90] Tefera, M., Chernet, T. and Haro, W. (1996). *Explanation of the geological map of Ethiopia (scale 1:2,000,000), technical report*. Ethiopian Inst. of Geol. Surv., Addis Ababa.

[91] Ukstins , I. A., Renne, P. R., Wolfenden, E., Baker, J. Ayalew, D. and Menzies, M. (2002). *Matching conjugate volcanic rifted margins; 40 Ar/ 39 Ar chronostratigraphy of pre- and syn-rift bimodal flood volcanism in Ethiopia and Yemen*. Earth and Planetary Science Letters, **198**: 289-306.

[92] Vinnik, L. K. (1977). *Detection of waves converted from P to SV in the mantel*. Phys.Earth.Planet.Int., **15**: 39-45

[93] Watanabe, T. (1993). *Effects of water and melt on seismic velocities and their application to characterization of seismic reflectors*. Geophys. Res. Lett., **20(24)**: 2933-2936.

[94] Wernicke, B. (1985). *Uniform sense normal simple shear of the continental lithosphere, Can*. J. Earth Sci., **22**: 108-125.

[95] Whaler, K. A., and Hautot, S. (2006). *The electrical resistivity structure of the crust beneath the northern Main Ethiopian Rift, in The Afar Volcanic Province Within the East African Rift System, edited by G. Yirgu, C. J. Ebinger, and P. K. H. Maguire*. Geol. Soc. Spec. Publ., **259**: 55-72.

[96] Wilson, D., Aster, R., Ni, J., Grand, S., West, M., Gao, W., Baldridge, W. and Semken, S. (2005). *Imaging the seismic structure of the crust and upper mantle beneath the Great Plains, Rio Grande Rift, and Colorado Plateau using receiver functions*. J. Geophys. Res., **110**: B05306, doi:10.1029/2004JB003492.

[97] WoldeGabriel, G., Aronson, J. L. and Walter, R. C. (1990). *Geology, geochronology and rift basin development in the central sector of the Main Ethiopian Rift*. Geol. Soc. Am. Bull., **102**: 439-458.

[98] Wolfenden, E., Ebinger, C., Yirgu, G., Deino, A. and Ayalew, D. (2004). *Evolution of the northern Main Ethiopian rift: birth of a triple junction, Earth Planet*. Sci. Lett., **224**: 213-228.

[99] Wolfenden, E., Ebinger, C., Yirgu, G., Renne, P. R. and Kelly, S. P. (2005). *Evolution of a volcanic rifted margin: Southern Red Sea, Ethiopia*. Geol. Soc. Am. Bull., **117**: 846-864.

[100] Zandat, C. and Owens, T.J. (1986). *Comparison of crustal velocity profiles Determined by Seismic Refraction and Teleseismic methods*. Tect. phys., **128**: 155-161

[101] Zandt, G. and Ammon, C. J. (1995). *Continental Crustal composition constrained by measurements of crustal Poisson's ratio*. Nature, **374**: 152-154.

[102] Zevallos, I., Assumpcao, M. and Padilha, A. (2009). *Inversion of teleseismic receiver function and magnetotelluric sounding to determine basement depth in the Parana Basin, SE Brazil*. J. Geophys., **68**:231-242

[103] Zhu, L. and Kanamori, H. (2000). *Moho Depth Variation in Southern California from Teleseismic Receiver Functions*. J. Geophys., **105**: 2969-2980.

APPENDIX A

COLLECTED DATA

Table A.1: Teleseismic events recorded in the four Ethiopian Broad Band Seismic Stations (ANKE, HARE, DILA and SEME) from September 2014 to June 2015

Day(Y/M/D)	Origin-Time (UTC)	Latitude(^{o})	Longitude(^{o})	Focal Depth(km)	Magnitude (mb)	Location of The Source Of Earthquake
2014/4/15	04:08:13	53.497	8.721	11.2	6.8	Bouvet Island Region
2014/4/19	13:47:44	6.755	155.024	43.4	7.5	SW Of Panguna Papua New Guinea
2014/7/11	19:35:21	37.005	142.452	20.0	6.5	East of Iwaki, Japan
2014/7/30	01:36:58	0.054	17.343	10.0	5.6	North of Ascension Island
2014/7/29	08:05:38	55.470	28.367	8.0	6.9	NNW of Visokoi Island
2014/8/18	02:37:24	32.703	47.695	10.2	5.6	Dehloran, Iran
2014/02/03	03:08:46	38.264	20.390	5.0	6.0	NNW Of Lixourion, Greece
2014/02/12	09:19:49	35.905	82.586	10.0	6.9	ESE Of Hotan, China
2014/02/24	23:26:55	4.131	62.877	4.0	5.6	Carlsberg Ridge
2014/04/15	03:57:01	53.497	8.722	11.2	6.8	Bouvet Island Region
2014/04/19	01:04:03	6.656	155.087	29.0	6.6	SW Of Panguna, Papua New Guinea
2014/04/19	01:04:03	6.656	155.087	29.0	6.6	SW Of Panguna, Papua New Guinea
2014/05/05	11:08:43	19.656	99.670	6.0	6.1	NNW Of Phan, Thailand
2014/05/18	01:02:32	4.248	92.757	35.0	6.0	West Coast Of Northern Sumatra

Day(Y/M/D)	Origin-Time (UTC)	Latitude(^{o})	Longitude(^{o})	Focal Depth(km)	Magnitude (mb)	Location of The Source Of Earthquake
2014/06/14	11:10:59	10.123	91.092	4.0	6.5	Southern Indian Ocean
2014/06/29	07:52:55	55.470	28.367	8.0	6.9	NWW Of Visokoi Island
2014/07/11	19:22:00	37.005	142.452	20.0	6.5	East Of Iwaki, Japan
2014/07/19	14:14:01	11.745	57.638	10.0	6.0	Owen Fracture Zone Region
2014/08/18	02:32:05	32.703	47.695	10.2	6.2	East Of Dehloran, Iran
2014/08/18	05:25:51	32.720	47.690	12.0	5.6	East Of Dehloran, Iran
2014/08/20	10:14:15	32.636	47.736	17.7	5.6	East Of Dehloran, Iran
2014/09/17	06:14:45	13.764	144.429	130.0	6.7	NW Of Piti Village, Guma
2014/10/17	02:14:31	32.108	110.811	16.5	7.0	SE Pacific Rise
2014/11/15	02:31:41	1.893	126.522	45.0	7.1	NW Of Kota Ternate, Indonesia
2014/11/21	10:10:19	2.300	127.056	35.0	6.5	WNW Of Tobelo, Indonesia
2014/4/01	23:46:47	19.610	70.769	25.0	8.2	NW of Iquique, Chile
2014/4/03	02:56:05	20.747	70.531	10.0	5.5	NW of Iquique, Chile
2014/04/11	07:07:23	6.586	155.048	60.5	7.1	WSW of panguna, Papua New
2014/6/29	07:52:55	55.470	28.367	8.00	6.9	NNW of Visokoi Island
2014/7/11	19:22:00	37.005	142.452	20.0	6.5	E of Iwaki, Japan
2014/7/03	01:07:47	37.459	78.154	20.0	6.4	SE of Yilkiqi, China
2014/7/27	21:41:21	2.629	138.528	48.0	7.0	W of Abepura, Indonesia
2014/9/16	22:54:32	31.573	71.674	22.4	8.3	W of Illapel, Chile
2015/2/13	18:59:12	52.649	31.902	16.7	7.1	N Mid Atlantic Ridge
2014/2/16	22:00:53	55.520	28.259	13.0	6.2	NNW of Visokoi Island
2014/2/20	04:25:23	39.824	143.587	10.0	6.2	E of Miyako, Japan
2015/2/16	22:24:12	55.520	28.259	13.0	6.2	NNW Of Visokoi Island

2015/2/16	23:19:52	38.856	142.881	23.0	6.7	ENE Of Miyako, Japan
2015/3/23	05:10:34	18.353	69.166	130.0	6.4	SSE Of Putre, Chile
2015/4/16	18:13:38	35.189	26.823	20	6.0	SW of Karpathos, Greece
2015/4/25	06:19:54	28.230	84.731	8.2	7.8	E Of Khudi, Nepal
2015/5/05	02:02:53	5.462	151.875	55.0	7.5	SSW Of Kokopo Papua New Guinea
2015/5/12	07:13:54	27.809	86.066	15.0	7.3	SE Of Kodaki Nepal
2015/5/12	21:26:11	39.906	142.032	35.0	6.8	SE Of Unato, Japan
2015/5/24	05:03:28	16.855	14.171	10.0	6.3	Southern Mid-Atlantic
2015/5/30	11:35:16	27.839	140.493	664.0	7.8	WNW Of Chichi-Shima, Japan
2015/6/17	13:02:57	35.364	17.160	10.0	7.0	Southern Mid-Atlantic Ridge
2015/7/03	01:15:55	37.459	78.154	20.0	6.4	SE Of Yilkiqi, China
2015/7/03	21:59:05	2.629	138.528	48.0	7.0	W Of Abepura, Indonesia
2015/9/18	16:12:11	15.277	45.989	10.0	6.0	Northern Mid-Atlantic
2015/02/13	18:59:12	52.649	31.902	16.7	7.1	Northern Mid-Atlantic
2015/02/16	22:00:53	55.520	28.259	13.0	6.2	NNW Of Visokoi Island, South georgia and South Sandwich
2015/02/16	23:06:28	39.856	142.881	23.0	6.7	ENE Of Miyako, Japan
2015/04/26	07:09:10	27.771	86.017	22.9	6.7	SSE of Kodari, Nepal
2015/05/12	07:05:19	27.809	86.066	15.0	7.3	SE of Kodari, Nepal
2015/04/26	07:09:10	27.771	86.017	22.9	6.7	SSE of Kodari, Nepal
2015/05/12	07:05:19	27.809	86.066	15.0	7.3	SE of Kodari, Nepal

Day(Y/M/D)	Origin-Time (UTC)	Latitude(^{o})	Longitude(^{o})	Focal Depth(km)	Magnitude (mb)	Location of The Source Of Earthquake
2015/05/12	21:12:58	38.906	142.032	35.0	6.8	SE Of Unato, Japan
2015/05/20	22:48:53	10.876	164.169	11.0	6.8	West Of Lata, Solomon Island
2015/05/22	21:45:19	11.056	163.696	11.2	6.9	ESE Of Kirakira, Solomon Island
2015/05/24	04:53:23	16.855	14.171	10.0	6.3	Southern Mid Atlantic Ridge
2015/05/30	11:23:02	27.839	140.493	664.0	7.8	WNN Of Chichi-Shima, Japan
2015/06/04	23:15:43	5.987	116.541	10.0	6.0	WNW Of Ranau, Malaysia
2015/06/04	23:15:43	5.987	116.541	10.0	6.0	WNW Of Ranau, Malaysia
2015/06/27	15:34:03	29.040	34.667	22.0	5.5	SSE Of Nuwaybi'a, Egypt
2015/07/03	01:07:47	37.459	78.154	20.0	6.4	SE Of Yilkiqi, China
2015/09/16	22:54:32	31.573	71.674	22.0	8.3	West Of Illapel, Chile
2015/09/24	15:53:27	0.621	131.262	18.0	6.6	North Of Sorong, Indonesia
2015/05/12	07:05:19	27.809	86.066	15.0	7.3	SE of Kodari, Nepal
2015/5/30	11:35:16	27.839	140.493	664.0	7.8	WNW Of Chichi-Shima, Japan
2015/05/12	07:05:19	27.809	86.066	15.0	7.3	SE of Kodari, Nepal
2015/05/12	21:12:58	38.906	142.032	35.0	6.8	SE Of Unato, Japan
2015/05/20	22:48:53	10.876	164.169	11.0	6.8	West Of Lata, Solomon Island
2015/05/22	21:45:19	11.056	163.696	11.2	6.9	ESE Of Kirakira, Solomon Island
2015/9/18	16:12:11	15.277	45.989	10.0	6.0	Northern Mid-Atlantic